REVIEW

All-inorganic perovskite nanocrystals: next-generation scintillation materials for high-resolution X-ray imaging

Lu Lu, Mingzi Sun, [iD] Tong Wu, Qiuyang Lu, Baian Chen and Bolong Huang [iD] *

With super strong penetrability, high-energy X-rays can be applied to probe the inner structure of target objects under nondestructive situations. Scintillation materials can down-convert X-rays into visible light, enabling the reception of photon signals and photoelectric conversion by common sensing arrays such as photomultiplier tubes and amorphous-Si photodiode matrixes. All-inorganic perovskite nanocrystals are emerging photovoltaic and scintillation materials, with tremendous light-conversion efficiency and tunable luminous properties, exhibiting great potential for high-quality X-ray imaging. Recent advancements in nanotechnology further accelerate the performance improvement of scintillation materials. In this review, we will provide a comprehensive overview of novel all-inorganic perovskite nano-scintillators in terms of potential applications in low-dose X-ray medical radiography. Compared with conventional scintillators, the merits/drawbacks, challenges, and scintillation performance control will be the focus of this article.

1. Introduction

X-ray is a kind of high energy electromagnetic radiation with ultra-strong penetrability, which can probe the inner situations under nondestructive testing.[1] It was first discovered by Wilhelm Röntgen in the year 1895,[2] and has been widely used in multiple fields such as medical radiography, photodynamic therapy (PDT), nuclear prevention and security inspection in recent decades.[3] The fundamental working principle of X-ray sensing is to monitor and reveal the attenuation of incident X-ray radiation after penetrating the specific targets. For instance, the intravital organ penetrating makes high-resolution radiography, which has been widely used in our daily life such as clinical diagnosis. The non-living objects penetrating enables industrial and security applications.[4] Currently, the modern X-ray detection techniques are generally classified into two categories: direct conversion from X-ray quanta to electrical signal *via* a semiconductor or to chemical signal *via* a film; and indirect conversion to low-energy photons (visible light) by scintillating materials.[1,5,6]

Up to now, for general X-ray imaging with integrating detectors, there are hardly any direct converting materials that can commercially replace nano-scintillators except for selenium (Se) detector for mammography.[6] Even the most competitive direct conversion materials with high resolution,[7] CdTe and CdZnTe (CZT), still suffer from low response rate and temporal effects

such as long afterglow caused by electron trapping.[1,6] Also, it is still difficult to manufacture a large-size wafer with a low noise current but high mobility-lifetime-product ($\mu\tau$), making it tough to achieve the acceptable price to performance ratio for commercial applications.[8] By contrast, scintillators can convert X-ray into visible light (down conversion), enabling the commercial applications of low-cost sensing arrays like photomultiplier tube (PMT), avalanche photodiode (APD),[9] amorphous-Si photodiode matrix, and charge-coupled devices.[10] Thus, emerging indirect conversion scintillating materials have attracted more research interests for X-ray sensing.

Conventional scintillators like $NaI:Tl^+$,[11,12] $CsI:Tl^+$, $CdWO_4$ (CWO),[13,14] $Bi_4Ge_3O_{12}$ (BGO),[11,12] Lu_2SiO_5 (LSO), and $Lu_{2(1-X)}Y_{2X}SiO_5$ (LYSO) have been commercially applied in medical imaging devices due to their high light output and strong stopping power. However, these materials still require further optimization to simplify the manufacturing processes, avoid the afterglow and achieve tunable scintillation by finding new electron-transition energy levels.[15–17] Especially for diagnostic radiology, realizing higher spatial resolution under lower dose radiation exposure is considered as the foremost appeal.[18,19] Owing to the attractive merits including easier fabrication, faster response, and higher spatial resolution, lead-halide perovskite nanocrystals based X-ray sensors are emerging to exhibit great application prospects in future radiography.[15,20] In terms of electronic properties, these halide perovskites usually have lower trap density,[21] higher charge-carrier mobility[22] and longer minority-carrier diffusion length,[23] peculiarly in nanocrystal morphology.[4,24,25]

Department of Applied Biology and Chemical Technology, The Hong Kong Polytechnic University, Hung Hom, Kowloon, Hong Kong SAR, China. E-mail: bhuang@polyu.edu.hk

With a fast response in a nanosecond, $CsPbCl_3$ was observed to have strong luminescence by free excitons when exposed to radiation, making it a promising scintillation material for X-ray detection in the late 20th century.[26] Whereas, the strong self-absorption, low photoluminescence quantum yield (PLQY), the toxicity of Pb, and poor stability of Pb-halide perovskites greatly limit their large-scale industrialization for X-ray medical imaging.[27] After decades of research, a series of Pb-free scintillators such as double-perovskite,[28,29] Cu,[30,31] and Bi[32]-based all-inorganic halide perovskites have been discovered that showed satisfying scintillation behaviors. For example, Rb_2-$CuBr_3$ (ref. 30) and $Cs_2NaTbCl_6$ (ref. 33) are popular Pb-free scintillators with high PLQY, however, the unfavored afterglow emission often causes reduced imaging contrast, and the impact is even worse in computed tomography (CT). The emission band of Rb_2CuBr_3 is peaked in the blue light range, not in the maximum sensitivity window of silicon photodetectors (peak photo-response in 700–900 nm). Thus, for realizing high contrast X-ray imaging, the exploration of Pb-free halide perovskite nano-scintillators with fast decay time and matched emission wavelength has been a recent research hotspot.

In this work, we have supplied a comprehensive review of recent achievements in the new generation of all-inorganic perovskite nano-scintillators for high-quality X-ray imaging. Firstly, the general working principle of X-ray detectors, scintillation mechanisms, and application criteria of scintillators for high resolution but low dose exposure X-ray imaging will be stated in detail. The mechanism of scintillation performance control based on native defects is one of the focuses. Then, the main merits/drawbacks, growth methods, performance, and applications of the emerging halide perovskite nano-scintillators are clarified. Recent breakthroughs and modification strategies on scintillation performance are demonstrated systematically. Comparisons of scintillation performance have been made between traditional and novel scintillators. Finally, we propose the remaining challenges of current all-inorganic perovskite nanocrystal scintillators for low-dose X-ray imaging to reach commercial applications. This review will provide insightful ideas for future scintillation material design and optimizations.

2. Scintillation mechanism

2.1 Working principle of X-ray detectors

Two conversion processes are mainly involved in the detection of X-ray: down-conversion of X-ray and photovoltaic conversion. As illustrated in Fig. 1a,[34] most commercial X-ray detectors share a universal design with three main functional layers: scintillator (X-ray absorption and conversion), photodiode arrays (photovoltaic conversion), and a substrate (for mechanical and electrical installation and keeping the structure flat). Firstly, the incident X-ray will be absorbed and converted into visible light in the scintillation layer, and the emission photons are further transformed into electric current in the photodiode matrix. The inversely biased photodiode will be pre-charged at a certain voltage and afterward discharged due to the photoinduced electron–hole pairs generated by the proton collision. The generated electrical signal will be transmitted to analog electronic devices for signal amplification in the substrate layer. At last, the magnified signal will be digitized and subsequently delivered from the detecting platform to acquisition circuitry for the formation of images.

The schematic framework of the frequently used amorphous-Si flat detector is indicated in Fig. 1b.[18] Generally, the scintillating material is $CsI:Tl^+$ due to the superior scintillation properties including matching emission spectrum with amorphous-silicon photodiodes, high absorption coefficient, and high light output. Through the vapor deposition, the $CsI:Tl^+$ scintillating crystal is formed in a needle-like structure in 5–10 μm diameter, with a length of ≥600 μm. This morphology can promote the collecting of emitted photons in the Si-photodiode matrix conjoined below. For modern multi-slice spiral CT scanners, an ultra-fast decay is the most important scintillation parameter. High-Z_{eff} scintillation crystals with a short afterglow lifetime like Gd_2O_2S (GOS) and Ce^{3+} doped $Lu_3Al_5O_{12}$ ($LuAG:Ce^{3+}$) are preferable for X-ray CT imaging.[18,35] Different from common flat detectors, a more discrete structure for scintillation layer construction is allowed in CT imaging with a relatively large pixel size so the scintillators are separated in angular and axial orientation. As a result, it enables the optical separation for individual pixels and at the same time spatially fits the Si-photodiode arrays.
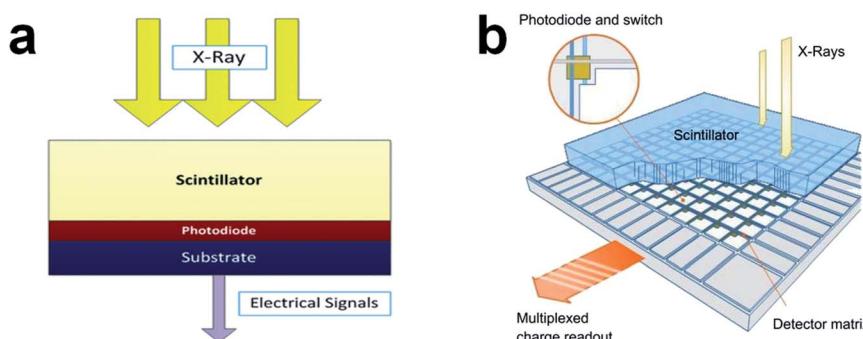

Fig. 1 (a) Schematic depiction of the three main functional layers in a common X-ray CT detector. Reproduced with permission.[34] Copyright 2013 Springer Nature Limited. (b) Schematic description of an X-ray flat detector constituted by columnar CsI:Tl+ scintillator and a detecting matrix of amorphous-silicon photodiodes. Reproduced with permission.[18] Copyright 2013 Elsevier.

2.2 Scintillation mechanism of common scintillating materials

Having a comprehensive understanding of the scintillating mechanism will benefit the optimization of existing scintillators as well as the design of next-generation scintillation materials. New experimental findings and emerging theoretical simulations will continuously benefit the advances of scintillating theory. Based on current findings and theoretical models, five main stages are involved in the whole scintillation process from initial X-ray excitation to final visible-light emission, and the schematic scintillation mechanism has been presented in Fig. 2.[36]

In the first stage, the initial excitations are produced by the interaction between ionizing particles and scintillators. The X-ray photons possess high energy, leading to the generation of deep holes (h^+) and hot electrons (e^-) in the inner core band and conduction band (CB), respectively. Followed by inelastic e–e scattering and auger process, h^+ in VB/core band and e^- in CB will be created rapidly by massive secondary electron excitation. The multiplicative stimulation for charge-carrier creation will be terminated at the end of this step. Along with the creation of phonons, the thermalization of electron excitation is the main concern in the next stage, resulting in the generation of low kinetic-energy e^- in CB minimum (CBM) and h^+ in VB maximum (VBM). Since the localization of electron excitation is usually accompanied by the replacement of atoms and photo-induced desorption, in the third stage, its interaction with native defects and external dopants/impurities in host lattice is the main feature. In the last two stages, charge carrier migration and the following radiative/nonradiative electron–hole recombination process is mainly involved. After final excitation *via* sequential charge-carrier capture or energy-transfer process, the last scintillation stage ends in the visible photon emission at the luminescent center. The interaction between electron excitations may cause reduction in their quantity, and it is considered as a decisive factor on material density-effect, non-exponential decay as well as nonproportional energy response.[36]
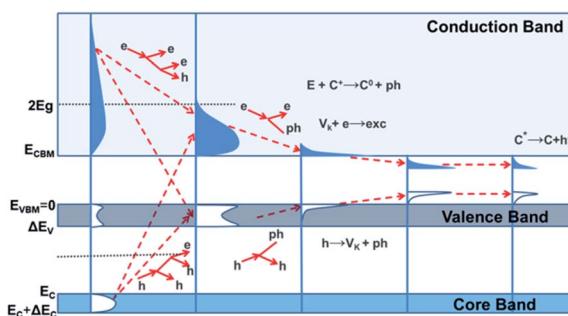
Fig. 2 Schematic mechanism explained by the relaxation of electron excitations in inorganic scintillation crystals. E_C refers to the top energy of core band, and ΔE_C represents the corresponding bandwidth; E_{VBM} refers to the top energy of VB ($E_{VBM} = 0$), and ΔE_V represents the bandwidth of VB; E_{CBM} refers to the bottom of CB, and E_g represents the bandgap. V_k means self-trapped holes, and C^+ represents ionic centers. Reproduced with permission.[36] Copyright 2017 Springer Nature Limited.

2.3 Scintillation performance control based on native defects

The electronic properties of defect states have strong impacts on material radiation stability and the production of persistent luminescence (PL). The formation of defects in host lattice is identified as the dominant cause for non-radiative energy losses in the scintillation process, including external dopants/impurities as well as intrinsic imperfections such as simple point defects (vacancies and interstitials), interfacial/surface states, and grain boundaries. Vacancy defects are very likely to be formed in fabrication processes particularly in heat treatments like annealing. Besides intrinsic point defects, the interaction between incident X-ray radiation and scintillation material also leads to the generation of lattice imperfection. Under X-ray excitation, with the vacancy formation in anionic sublattice, it is very common for inorganic oxide scintillators to have defects particularly when the dopant/impurity ions have different charge states from those in initial lattice sites. If the electronic energy states of defects appear below CBM and with a certain trap depth, the photo-induced electrons will be trapped and have delayed recombination with the relaxed holes at the luminescent center.[37] The prolonged scintillation decay time will cause a severe negative influence on imaging contrast in high-speed CT scanning.

Having severe impacts on thermal conductivity and ionic conduction,[38–40] the anion Frenkel (a-Fr) defects serve as the dominant imperfection type in fluorides and oxides lattice, formed by an anion moving from its original site to a neighboring interstitial site, resulting in an uncharged vacancy-interstitial defect pair in the lattice.[38,39,41,42] The migrating charge carriers can be trapped and stored in these defect states, mainly in those of vacancies. The electrons/holes in traps will be released by ambient thermal disturbance, followed by phonon-assisted migration.[43] It is energetically preferable for these electrons/holes to be transferred from the de-localized CB to localized states within the bandgap *via* phonon coupling, which leads to decreased transmitting rate of polarons. Thus, by restraining the formation of defects, the mobility of charge carriers can be accelerated, and the recombination delay, as well as the non-radiative energy losses will be shortened. The advancements in crystal growth technology and optimization in material morphology are expected to suppress the emergence of imperfections in host lattice, so the scintillating transport state can be significantly tuned by material manufacturing process control.[44]

It has been reported that the addition of co-dopants can suppress afterglow emission,[45–47] but with drawbacks in lowered light yield.[48] For instance, Ce^{3+} co-dopant can efficiently restrain the afterglow emission of GOS:Pr^{3+} and GOS:Tb^{3+}, but it suffers a remarkable reduction in light output at relatively low temperatures.[49] It should be noted that the addition of co-dopant ions will make an intentional compensation for intrinsic defects, but the total concentration of defects cannot be decreased. The lattice imperfections that do not have impacts on scintillating properties are expected to displace those detrimental ones under specific conditions. Thus, the

potential influences that the dopants may make on defect formation should be fully understood for further scintillation performance modulation.[46]

Modern computational simulation technology can well reveal the structural and electronic properties of defects, so it is very promising for the design and performance optimization of next-generation scintillators. For example, the $NaYF_4$ is a potential scintillation material, but its long afterglow will limit its application in high-resolution CT imaging.[3] In our previous work, to reveal the PL mechanism of $NaYF_4$, the electronic defect states in the bandgap are fully investigated by DFT calculation under the CASTEP code.[50] The PL can be suppressed by facilitating the non-radiative recombination by applying specific doping schemes or defect states modulation based bandgap engineering.[3,47,51,52] Based on the electronic properties including the distribution of defect states in host bandgap, the computational simulation can provide researchers with comprehensive theoretical support on finding potential co-dopants for PL elimination.

3. Requirements for X-ray scintillation imaging

Based on their unique down-conversion capacity (converting high-energy X-ray/γ-ray into visible light), scintillators have been widely used in nuclear security,[16] medical imageology,[53–55] and PDT.[56,57] Since the intrinsic factors of scintillators have a direct impact on detection efficiency, the performance parameter requirements for these scintillating materials vary from different application fields. For the applications in homeland security, diffusely deployed sensing systems for γ-ray spectroscopy are the fundamental requirement. Consequently, energy resolution becomes the main concern. For X-ray CT imaging, current challenges focus on achieving higher conversion efficiency and spatial resolution, faster response, and avoiding afterglow for scintillator development. To this end, the key performance parameters of scintillators and the corresponding effects on detection efficiency, especially in terms of CT imaging, are discussed in the following sections.

3.1 Main parameters of common scintillators

(1) Conversion efficiency. The quantity of emission visible-light photon (N_{ph}) generated during scintillating conversion process by per energy (E) of incident X-ray photon is expressed by the following formula:[58]

$$N_{ph} = \{E/(\beta E_g)\}SQ \tag{1}$$

β is the phenomenological parameter, generally in the range of 2–3; E_g represents band-gap value; S refers to transfer quantum efficiency; and Q is the quantum efficiency of emission center. The corresponding efficiency η has been expressed by the formula as follows, where E_{vis} stands for the photon energy of emission visible light.[58]

$$\eta = E_{vis}N_{ph}/E \tag{2}$$

(2) Light yield (LY). LY (in photons per MeV) is a key parameter for the description of scintillating efficiency, can be expressed by the following equation:[36]

$$LY = (10^6/\beta E_g)SQ \tag{3}$$

in which E_g represents the bandgap value (in eV), $\beta = E_{e-h}/E_g$, E_{e-h} represents the energy consumption for producing an electron–hole pair; S and Q refer to the quantum efficiency of transport and luminescence stage respectively.

(3) Decay time. The decay time is the duration time that the scintillators emit ultraviolet (UV)/visible light after the absorption of the incident X-ray energy. Short decay/fast response is essential for fast-scan imaging. In general, the quenching process can reduce decay time but cause a decline in LY.

(4) Stopping power. With fixed thickness, the attenuation coefficient relies on material density (ρ) and atomic number (Z_{eff}). Thus, the stopping power is in direct proportion to ρZ_{eff}.[58]

(5) Matching emission spectrum with the photodetector. To reduce post-scintillating loss, the radioluminescence spectrum should be well overlapped by the peak response window of the photodetector. For instance, scintillation emission in the visible/near-infrared (NIR) region to match the optimal detection sensitivity of silicon photodetector.

(6) Chemical stability. The chemical stability is largely affected by hygroscopicity, which is a key parameter that evaluates the material lifespan.

(7) Radiation hardness. This indicates the capacity that the scintillating performance remains undecayed under high-energy X-ray/γ-ray radiation. Although radiation hardness is a key property concerned in high-power physics,[59] it shows the limited effect on common medical imaging.

(8) Proportionality. This parameter has an obvious impact on intensity identification ability, so linear scintillation response is required.

(9) Spatial resolution. It reveals the contrast ratio and the number of blurs (image sharpness) under a specific spatial frequency, which can be calculated by the modulation transfer function (MTF).[60]

3.2 Specific requirements for X-ray CT imaging

Integrated down-conversion scintillators are generally employed by modern digital X-ray imaging apparatuses and CT scanners to optically match the peak sensitivity window of the Si p-i-n photodiode matrix. The exposure dose has been the first concern, so the scintillators must have enough stopping power to absorb almost all of the incident X-ray energy. That is, for a given imaging resolution, the radiation dose is required to be as low as possible. For example, the thin ceramic scintillator screen (0.1–0.2 mm) can satisfy the lowest X-ray energy detection (around 20 keV in mammography). In dental radiography (around 60 keV) and full-body CT scanning (approximate 150 keV), a thicker scintillator screen is needed. With better transparency, mono-crystalline scintillation materials are thus employed instead of ceramic counterparts. Modern CT scanners need to record nearly 1000 slices per second, *via* memory effect,

Table 1 Summary of the key parameters for scintillators in X-ray imaging, from typical representatives to novel Pb-free perovskites

Scintillator	Density (g cm^{-3})	Peak emission (nm)	Light yield (ph per MeV)	Decay time (ns)	Afterglow	References
NaI:Tl$^+$	3.67	415	38 000–55 000	250	—	11 and 12
BGO	7.13	480	8000–10 000	300	—	11 and 12
LYSO:Ce^{3+}	7.1–7.2	420	30 000–33 000	45	—	11
CWO	7.9	495	28 000	5000	0.05% after 3 ms	13 and 14
GOS:Pr^{3+}, Ce^{3+}, F$^-$	7.34	520	50 000	2400	<0.1% after 3 ms	13
GOS:Tb^{3+}, Ce^{3+}	7.34	550	50 000	6×10^5	0.6% after 3 ms	13
CsPbBr$_3$	—	525	21 000	8.09	—	73
Cs$_3$Cu$_2$I$_5$:Tl$^+$	—	440, 510	87 000	957, 717	0.17% at 10 ms	112
Cs$_2$Ag$_{0.6}$Na$_{0.4}$In$_{1-y}$Bi$_y$Cl$_6$	—	605–652	39 000 ± 7000	1	0.1% at 16 μs	27

afterglow emission will cause unwanted ghost images, thus ultra-fast decay is required. Based on these special requirements in terms of clinic application, the key parameter criteria for scintillators used in X-ray CT imaging are summarized below:[13,61]

(1) **High absorption coefficient.** For a reliable reference for clinical diagnosis, the imaging contrast must reach a certain level, thus a certain amount of exposure dose cannot be avoided. Promotion in scintillating efficiency can remarkably cut down the necessary radiation dose for an acceptable CT image quality.[62] To guarantee reasonable image quality at a suitable radiation dose exposure on the patient, the absorption coefficient should approach 100% at about 2 mm thickness.

(2) **High light yield.** For image noise elimination especially at the low signal level, light yield >20 000 photons per MeV is a particularly attractive scintillation parameter.[13]

(3) **Fast decay.** To track the signal variation produced under sub-0.5 s scan time, scintillating materials with ultra-fast decay time is required for X-ray CT detectors, generally <1 ms is acceptable.[61] But in fact, to match the projection sampling rate (at ≥10 kHz) of modern CT scanners, the decay time should achieve at least 1–10 μs range.[13]

(4) **Weak scintillation afterglow.** This parameter is expressed by the percentage of X-rays that remain 3 ms after the turned-off of continuous X-ray radiation, with a desirable value of <0.1%.[13] For CT applications, the elimination of afterglow is the most effective means to avoid sickle artifacts.

(5) **Small thermal coefficient of light output.** The thermal light coefficient reveals the variation in light yield under temperature fluctuation, ideally to be in the ±0.1% per °C range.[13]

(6) **Matching radioluminescence spectrum.** For CT imaging, Si-photodetectors are generally applied. In view of this, the ideal peak scintillation emission wavelength is within 400–900 nm to match the maximum spectral sensitivity of photodiode arrays.[63]

4. Scintillation materials

Due to the superior and tunable scintillating properties, rare earth (RE) doped nanocrystals are widely applied in X-ray imaging.[16,64] For CT applications, by bandgap engineering or specific doping strategy, fast-decay scintillation in microsecond/nanosecond magnitude with weak afterglow can be achieved.

The emission originates from the 5d–4f/4f–4f transition of doped RE ions are generally located in the visible light region (green-yellow), matching well with the sensitive readout range of common photodiodes. Due to the spin and parity allowed 5d–4f transition, intense scintillation emission can be produced from the Ce^{3+} center, with a relatively fast decay in nanosecond order. Eu^{2+}, Er^{3+}, Ho^{3+}, Tm^{3+}, and Pr^{3+} are also commonly used RE-dopants because of their wide emission bands (visible-NIR) that are generated by the fast 4f–4f transition in several microseconds.[52]

The energy resolution is identified as a crucial performance parameter required for practical X-ray scintillation imaging applications. Eu^{2+}-doped halide scintillation materials such as SrI$_2$:Eu^{2+} and CsBa$_2$I$_5$:Eu^{2+} not only exhibit high energy resolution but also have high LY because quenching will not happen though Eu^{2+} doping has achieved a high ionic concentration.[65–67] Whereas the adverse reabsorption caused by self-absorption of surrounding Eu^{2+} will become worse if the doping concentration is too high. As a result, scintillation performance including LY, energy resolution as well as decay time will all be affected.[65] A novel strategy has been reported to reduce the reabsorption effects by low-concentration co-doping ions such as Sm^{2+} that can absorb Eu^{2+}emission but re-emit it in a higher NIR window.[68,69] CsBa$_2$I$_5$:Eu^{2+}, Sm^{2+} is one of the successful cases, by shifting the emission wavelength to NIR range, a relatively high energy resolution of 3.2% (under 662 keV γ-ray, APD detector) can be realized.[9]

Metal-halide perovskites are emerging photovoltaic materials, with tremendous light-conversion efficiency and adjustable luminous properties.[70–73] Besides promising applications in solar cells,[74] they are also potential scintillation materials for X-ray/γ-ray detection, among which lead halide perovskite is the most typical representative.[15,73] However, the light output of this type of materials such as CsPbBr$_3$ nanocrystal is only 21 000 photons per MeV,[73] much lower than conventional scintillators like GOS:Pr (50 000 photons per MeV) and CsI:Tl (66 000 photons per MeV).[75] Small stokes-shift and strong self-absorption are reported to be the main causes for the limited light yield of Pb-halide perovskite thin-films/nanocrystals.[76,77] And from the perspectives of environmental protection and sustainable development, the practical applications of Pb-halide perovskites will be severely restricted due to the toxicity of Pb and the material instability.[78] Thus, developing stable Pb-

free perovskites with high PLQY becomes a new research hot-spot.[27,77] The summary of the key parameters for various scintillators from conventional materials to recent Pb-free perovskites in X-ray imaging has been indicated in Table 1.

4.1 Rare-earth doped scintillators

Long-lasting phosphorescent materials can gradually de-trap the stored electrons for long afterglow emission, facilitating the development of flat-panel free detector for X-rays.[64] Transition metal/RE doped inorganic oxides like W(vi)-doped ZnGa$_2$O$_4$:Cr^{3+} and Eu^{3+}-doped NaGdF$_4$ have already been applied for *in vivo* X-ray imaging, but they still exhibit relatively poor X-ray sensitivity.[79,80] In addition, the manufacturing technology for crystal growth is complicated. In particular, for the formation of abundant electron trapping states within the host bandgap, high synthesis temperature over 600 °C is required.[81] Benefit

from the rapid development of nanotechnology, nanoscale lanthanide scintillators are successfully fabricated for X-ray conversion.[64,82] Recently, a novel Tb^{3+}-doped NaLuF$_4$ nano-scintillator has been reported to have high X-ray absorption efficiency and super-long light emission lifetime, making it possible for flat-panel free X-ray 3D imaging for highly curved objects, see Fig. 3a–f.[64] The outstanding X-ray conversion and long-term electron storage ability can be explained by the defects formation under high energy excitation (Fig. 3g and h). Small anions have migrated from their original lattice sites to interstitial sites, resulting in vacancy-interstitial defect pairs as Frenkel defects.[83]

Another novel RE-doped scintillation nanocomposite (core–shell–shell structured NaLuF$_4$:Gd, Eu@NaLuF$_4$:Gd@NaLuF$_4$:Gd, Tb) has been reported to have dual functions for PDT and X-ray imaging, as shown in Fig. 4a.[82] Under X-ray irradiation,
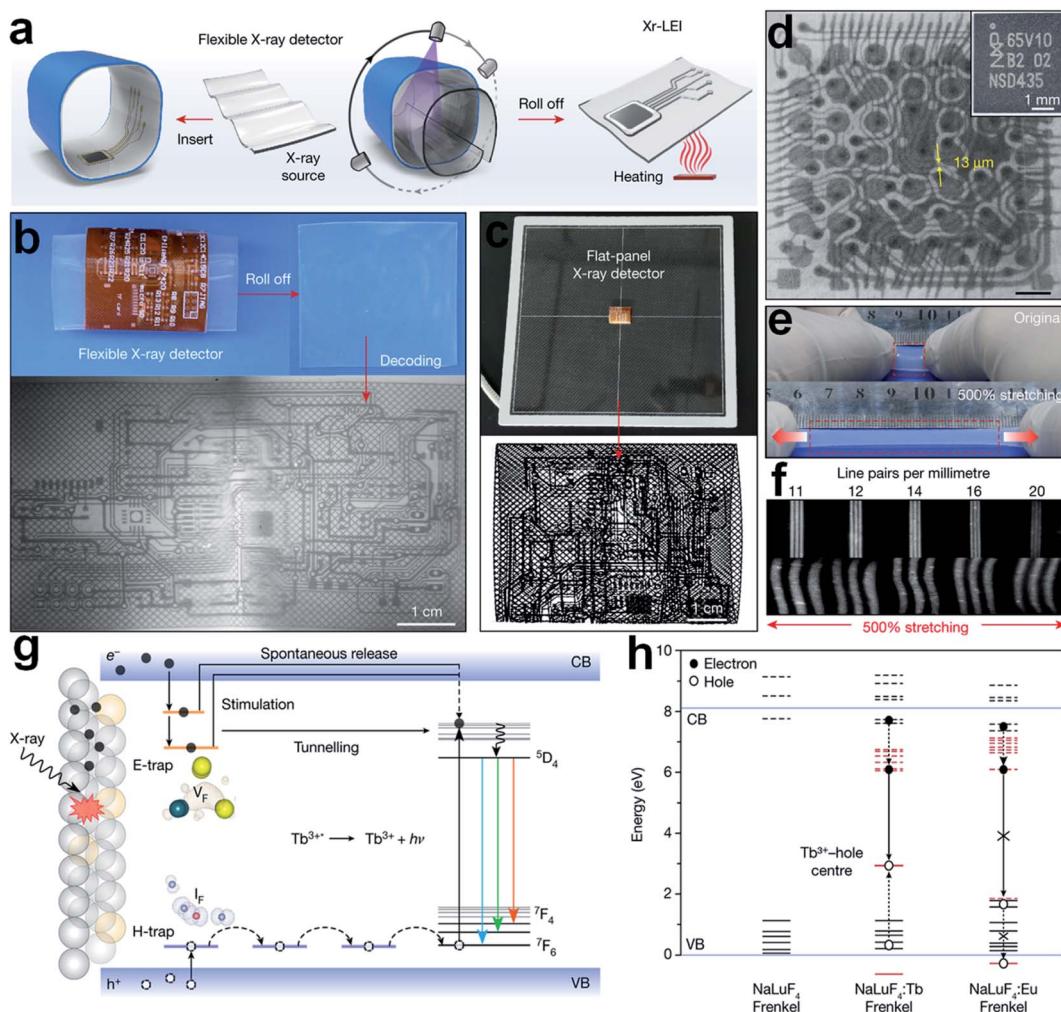

Fig. 3 (a) Schematic description of three-dimensional (3D) electronic scintillation imaging through nanoparticles based stretchable X-ray detector. (b) X-ray luminescence extension imaging (Xr-LEI) of a 3D circuit board by the NaLuF$_4$:Tb^{3+}(15 mol%)@NaYF$_4$ based flexible X-ray detector (50 kV, 80 °C). (c) X-ray imaging on the same electronic board by a traditional packaged flat panel detector. (d) Xr-LEI of inner circuits of an iPhone. Inset: digital photo of the same integrated circuits. (e) Photograph of the flexible scintillation layer. (f) High-quality Xr-LEI by applying the flexible X-ray detector. (g) Mechanism of long lifetime scintillation emitting of NaLuF$_4$:Tb^{3+} nanocrystals. (h) Energy diagram of lanthanide 4f levels (in red) with reference to host bands (in black). Solid and dotted lines indicate occupied and empty states, respectively. Reproduced with permission.[64] Copyright 2021 Springer Nature Limited.
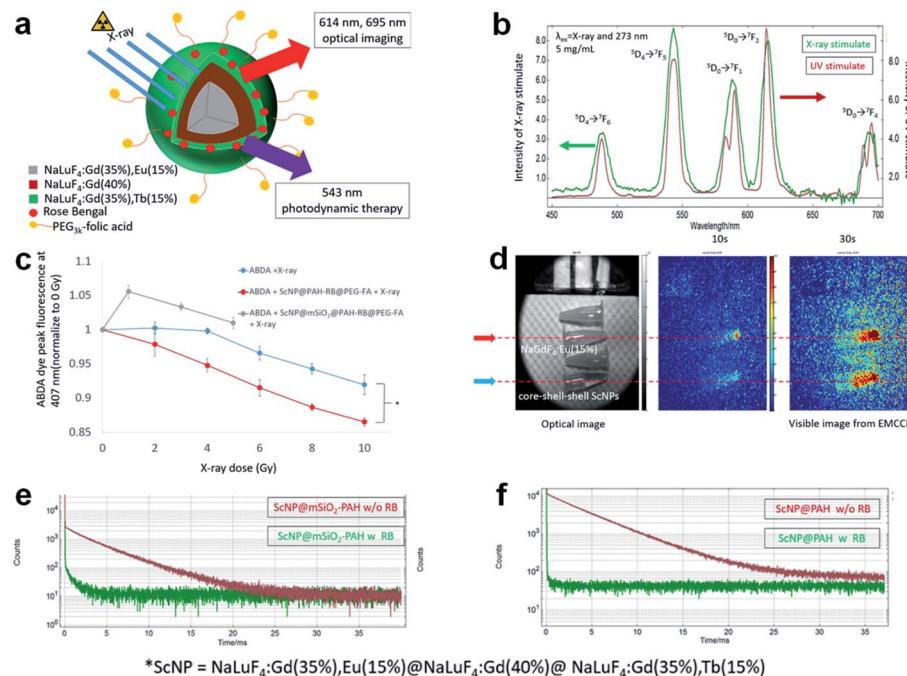
Fig. 4 (a) Schematic description of novel RE-doped scintillation nanocomposite (core–shell–shell structured NaLuF$_4$:Gd, Eu@NaLuF$_4$:-Gd@NaLuF$_4$:Gd, Tb) for X-ray imaging and PDT. (b) Emission spectra of the core–shell–shell scintillator nanoparticle (ScNP) under X-ray/UV irradiation. (c) $^1O_2$ generation test under X-ray radiation. (d) X-ray induced luminescence by a homemade fluorescence/computed tomography (FT-CT) device. (e) Exponential decay curves of Tb^{3+} $^5D_4 \rightarrow {}^7F_5$ transition before and after the loading of Rose-Bengal: ScNP@mSiO$_2$–poly(-allylamine) and (f) ScNP–poly(allylamine). Reproduced with permission.[82] Copyright 2018 American Chemical Society.

visible light emissions can be generated from the Tb^{3+} center (543 nm), stimulating the pre-loaded photosensitizer (Rose-Bengal). With the formation of $^1O_2$, the target cancer cells will be killed efficiently (see Fig. 4b and c). Meanwhile, the incident X-ray can be down-converted to visible emission from the recombination center of Eu^{3+} (614 nm and 695 nm), making the scintillation imaging possible (see Fig. 4b and d). The decay time is sharply declined from 4243 µS to 29 µS with the loading of Rose-Bengal due to the energy transfer (ET) from Tb^{3+} to Rose-Bengal. But this rate of decay still cannot satisfy the requirement of high-speed CT scanning (see Fig. 4e and f).

4.2 All-inorganic Pb-halide perovskite scintillators

With an ultra-high solar-to-energy power conversion efficiency of over 20%, perovskites photovoltaic materials are recent research focus in solar cells,[84,85] photoelectric sensors,[86] X-ray/γ-ray detection.[87–90] After a decade of development, depending on the innovation in film-growth technique and interface engineering, the photoelectric conversion efficiency of organic–inorganic perovskites-based solar cells has dramatically increased from 3.8% to 25.2%.[91–93] Whereas, the intrinsic thermal instability of these hybrid perovskites, in organic–inorganic absorbing/organic charge-migrating layer, severely limits their extensive commercial applications.[94] Fortunately, all-inorganic perovskites (such as CsPbI$_3$ and CsPbI$_2$Br) are identified that exhibited better thermal stability,[95] attracting intense research attention in recent years. And the material stability under high-energy radiation is found to be promoted

obviously when the organic cations (MA$^+$ or FA$^+$) in hybrid perovskites are substituted by Cs$^+$.[88] The high-Z_{eff} effect of Cs$^+$ based perovskites exhibit better X-ray absorption capacity in equivalent thickness to organic cations based counterparts. In addition, the electrical resistivity of all-inorganic Pb-halide perovskites is generally higher than that of organic ones, which contributes to a lower dark current.[96] Based on the factors mentioned above, all-inorganic perovskites are more promising materials for X-ray scintillation.

During the past three decades, the scintillating properties of all-inorganic Pb-halide perovskites have been deeply investigated.[26] Early single-crystal CsPbCl$_3$ exhibits a quite low light output of 320 photons per MeV, not capable of practical scintillation applications.[97] Subsequently, single-crystal CsPbBr$_3$ has been synthesized, with a high light-output (40 000–60 000 photons per MeV) under 12 keV X-ray excitation and an ultra-fast response (1 ns) at the low ambient temperature of 7 K.[98] However, the evaluation reports on their room-temperature scintillation properties are very rare in early research. Since 2015, halide perovskite CsPbX$_3$ (X= Cl, Br, I, or mixed-halide systems) nano-scintillators have been synthesized via hot-injection method, realizing a high PLQY up to 90%, a fast-decay of 1–29 ns, and tenable emission in the whole visible range (410–700 nm).[99] From then on, all-inorganic Pb-halide perovskite nanocrystals have been intensely investigated for X-ray scintillation detection.

In terms of X-ray scintillating applications, material stability under high-power radiation is also a fundamental factor for

medical detector construction. Various all-inorganic Pb-halide perovskites have attracted increasing research interests in scintillation applications due to their fast response and high detection efficiency to X-rays.[100] Generally, bulk all-inorganic Pb-halide perovskites are manufactured by the Czochralski method, under an ambient temperature of over 1700 °C.[101] Whereas, single-crystal perovskite scintillators are very sensitive to ambient humidity and exhibit limited stability in air.[67] To achieve satisfactory X-ray scintillation performance, a low temperature below 130 K is needed.[1] Benefiting from the development of nanotechnology, for further scintillation-property modification, researchers are inspired to shrink the material size down to the nanoscale.[54,102,103] The emerging nanoscale perovskites are discovered that have good process-ability in the fabrication of scintillation thin-film, which is favorable for the construction of flexible devices.[103] Besides, due to quantum and small-size effects, perovskite nano-scintillators exhibit distinctive electromagnetic and highly-expanded optical features.[104] It should be also noted that on the one hand the material minification into nanoscale can bring about highly improved scintillation property but on the other hand it causes a decrease in effective mass density, and thus reduce the stopping power. Fortunately, researchers have found effective solutions for this problem by new material fabrication technology. For instance, under high-energy X-ray irradiation, the nano-scintillator $CsPbCl_{3-X}Br_X$ will easily decompose so it is not capable of long-term operation.[105] Through blade coating technology, a large-scale all-inorganic perovskite film ($CsPbBr_3$/Cs_4PbBr_6) has been successfully fabricated to function as an imaging screen, exhibiting good stability to resist radiation damage and humidity in air.[106]

Recently, a novel commercializable $CsPbBr_3$ perovskite nano-scintillator with high-performance and low cost has been reported for non-destructive X-ray imaging (Fig. 5a and b).[107] It has been identified that the proposed $CsPbBr_3$ perovskite nanocrystal film has superior scintillation properties than
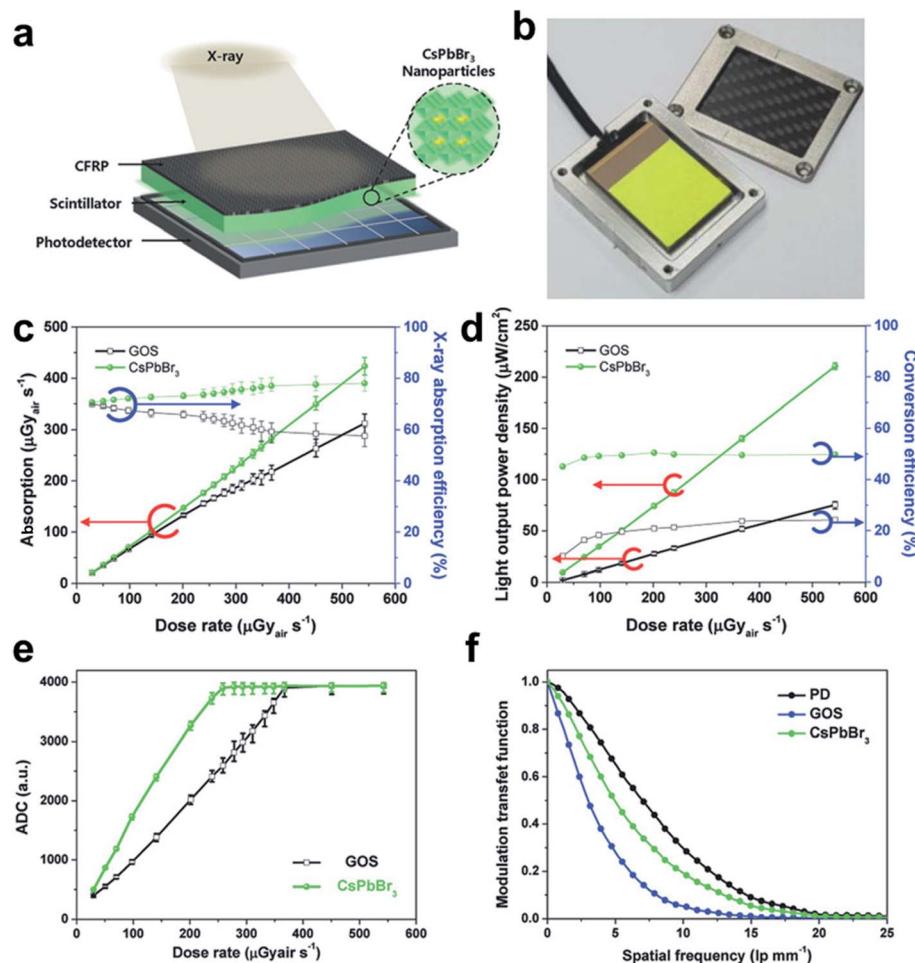

Fig. 5 (a) Schematic $CsPbBr_3$ perovskite nanoparticles-based X-ray detector. (b) Photograph of the $CsPbBr_3$ perovskite nano-scintillator film on a Si-photodetector module. (c) Comparisons on X-ray absorption efficiency of $CsPbBr_3$ perovskite nanocrystal and commercialized GOS scintillator. (d) Scintillation performance comparison for $CsPbBr_3$ and GOS on light output power density and X-ray conversion efficiency. (e) Analog to digital converted (ADC) values under various X-ray dose rates by $CsPbBr_3$ and GOS scintillation respectively. (f) Modulation transfer function of pristine Si-photodetector, $CsPbBr_3$ perovskite nano-scintillator, and traditional GOS scintillator based X-ray detection. Reproduced with permission.[107] Copyright 2018 Wiley-VCH.

conventional GOS film. As indicated in Fig. 5c and d, both the X-ray sensitivity and absorption efficiency of $CsPbBr_3$ are much higher than that of GOS. We can also find that the light-yield power density and absorption efficiency for both samples are in a good linear correlation with the imposed dose rate. On the other side, it is obvious that the $CsPbBr_3$ counterpart is more sensitive to X-ray radiation. The X-ray conversion efficiency of $CsPbBr_3$ has reached 45–49%, more than twice of commercialized GOS. The practical scintillation performances of both films are also tested by applying them as scintillator layers in an X-ray detector. As seen from Fig. 5e and f, owing to its outstanding spatial resolution, higher image resolution can be obtained from $CsPbBr_3$ nano-scintillator based X-ray detector than that sensed by GOS scintillation, particularly at relatively low radiation dose.

Another successful perovskite $CsPbBr_3$ nanocrystal scintillator has also been reported that have sharp and tunable light emissions over the visible spectrum range, making it capable of high-quality X-ray imaging in the common digital camera (Fig. 6a and b).[15] Furthermore, under relatively low dose
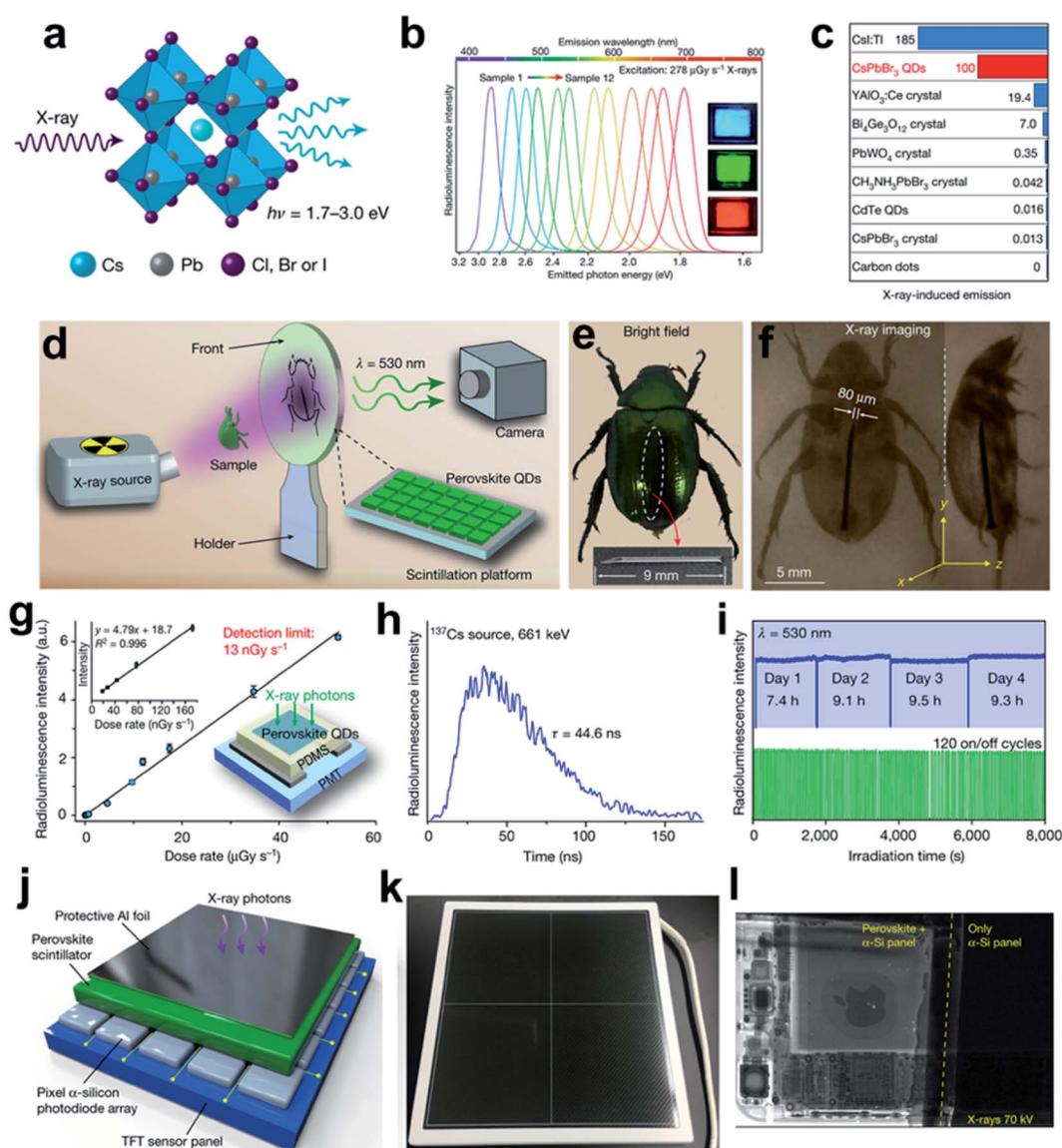
Fig. 6 (a) Schematic description of X-ray radioluminescence (RL) produced in a cubic all-inorganic perovskite lattice. (b) Tunable emission wavelength of the $CsPbX_3$ perovskite quantum dots under X-ray excitation (278 µGy S^{-1}, 50 kV). (c) Comparisons of the optical sensitivity on different scintillators under 10 kV X-ray excitation. (d) Flow chart for real time X-ray scintillation bio-imaging. (e) Bright field and (f) X-ray imaging recorded by a common digital camera. (g) RL intensity of $CsPbBr_3$ in response to various X-ray dose rates. Inset: RL intensity at low-dose rates (left) and schematic $CsPbBr_3$ nano-scintillator thin-film based X-ray detector (right). (h) RL decay curves of $CsPbBr_3$ nano-scintillator. (i) Photostability tests for $CsPbBr_3$ nanocrystal under continuous and repeated cycles X-ray exposure. (j) Multilayered design of the flat panel X-ray imaging platform constituted by a thin-film transistor sensing panel, a pixelated α-Si photodiode array, a $CsPbBr_3$ nano-scintillator thin film, and a protective Al-foil cover. (k) The packaged flat panel X-ray photodetector. (l) Comparison of X-ray images of an iPhone obtained with (left) and without (right) the perovskite $CsPbBr_3$ nano-scintillator. Reproduced with permission.[15] Copyright 2018 Springer Nature Limited.

radiation of 5.0 μGy s^{-1}, the optical sensitivity of $CsPbBr_3$ nano-scintillator film (0.1 mm) still exhibits comparability to that of typical CsI:Tl bulk single crystal (5.0 mm). And the X-ray conversion efficiency is five or even dozens of times higher than those conventional scintillation crystals such as $YAlO_3$:Ce, BGO, and $PbWO_4$ (see Fig. 6c). In phase-contrast imaging application, since the stopping power of metal and insect-tissue for X-ray is very different, a high-contrast image of the beetle body with a metal needle inside can be obtained over the background of $CsPbBr_3$ nano-scintillator substrate film (Fig. 6d–f). For clinical uses, exploring novel materials or methods for further decreasing the imposed dose rate with satisfactory imaging resolution is highly significant for the reduction of radiation injury.[37] In this work, an ultra-low detection limit of 13 nGy s^{-1} has been achieved, with a radiation dose more than 400 times lower than that used in common X-ray diagnostics (Fig. 6g).[108] Besides, with good photostability, the proposed nano-scintillator exhibits a relatively rapid response in 44.6 ns, indicating its potential in high-speed CT scanning (Fig. 6h and i). The suitability for the construction of a flat-panel X-ray detector has also been evaluated (Fig. 6j and k). The light scattering in nanocrystal thin-film substrate is much lower than that in typical micropillar/polycrystalline ceramic based bulk scintillators, which contributes to higher spatial resolution. As indicated in Fig. 6l, the inner structure of electronic circuit in an iPhone has been clearly imaged under low radiation dose (15 μGy). To sum up, this perovskite $CsPbBr_3$ nanocrystal scintillator is a very promising candidate for future radiographic diagnosis under low-dose exposure.

4.3 Lead-free halide perovskite scintillators

As illustrated above, the novel Pb-halide perovskite nano-scintillators ($CsPbX_3$) have exhibited their assets of facile manufacture, high conversion efficiency, high spatial resolution, good photo-stability and fast response.[15,89,107] Whereas, these nanoscale scintillators still suffer relatively low light-output, poor stability, and the toxicity of Pb, which imposes a great restriction on their practical utilization in low-dose radiographic diagnosis.[27] Recently, a series of Pb-free halide perovskite scintillators based on substitutional metal ions such as Cu,[31,76,109–112] Bi,[32,113,114] and double perovskites[27,29,115] have revealed improved scintillation performance, featuring environmentally friendly fabrication. Among them, although Rb_2-$CuBr_3$ (ref. 76) and $Cs_2NaTbCl_6$ (ref. 33) display high radioluminescence output, the intense PL severely limits their applications in CT imaging. And the emission band of the proposed Rb_2CuBr_3 scintillator is located in the blue-light range, mismatching the peak sensitivity of a standard digital camera. Thus, the exploration of Pb-free halide perovskite scintillators characterized with high light output, short decay time, as well as applicable/tunable emission wavelength is deemed to be a promising research orientation.

In a recent report, a novel Pb-free double-perovskite single-crystal $Cs_2Ag_{0.6}Na_{0.4}In_{1-Y}Bi_YCl_6$ (Fig. 7a) are synthesized and tested to have an improved light yield of 32 000–46 000 photons per MeV and a super short decay time of 1 ns when in Cs_2-$Ag_{0.6}Na_{0.4}In_{0.85}Bi_{0.15}Cl_6$ form, due to the accelerating radiative recombination triggered by the appropriate concentration of Bi^{3+} dopant ($Y = 0.15$).[27] This perovskite scintillator shows
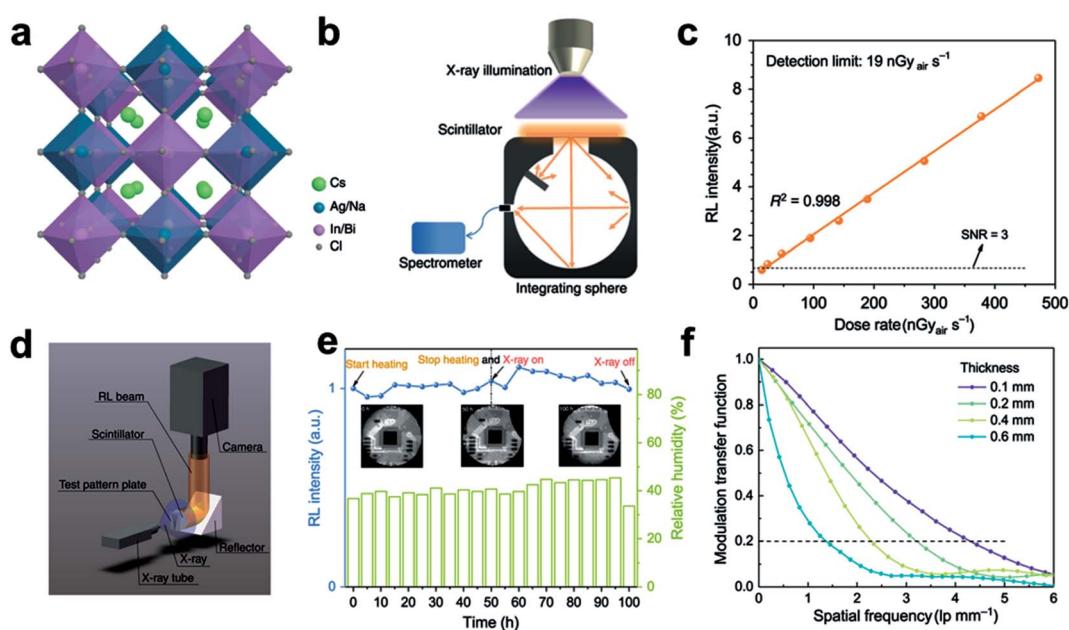

Fig. 7 (a) Crystal structure of the novel Pb-free double perovskite ($Cs_2Ag_{0.6}Na_{0.4}In_{0.85}Bi_{0.15}Cl_6$). (b) Schematic radioluminescence (RL) spectra by an integrating sphere as well as a spectrometer with a constant distance from X-ray source to object. (c) RL intensity of the proposed double perovskite detected at low-dose rates. (d) Schematic X-ray imaging platform. (e) Integrated RL intensity of the proposed double perovskite under thermal treatment (50 h at 85 °C) followed by X-ray irradiation for another 50 h (12 μGy$_{air}$ S^{-1}, 50 kV). (f) Modulation transfer function curves of the proposed double perovskite wafers with different thicknesses. Reproduced with permission.[27] Copyright 2020 Springer Nature Limited.

a good radiation stability as well as long-term thermal and chemical stability in air. High-resolution images of various objects can also be attained by low-dose radiation exposure (47.2 μGy S^{-1} for dynamic and 1 μGy for static imaging), indicating its potential applications in clinic radiography use (Fig. 7b–f).

Recently, low-dimensional especially zero-dimensional (0D) perovskite materials have addressed intense attention due to their outstanding scintillation properties for future optoelectronic and RL imaging applications. A 0D Pb-free $Cs_3Cu_2I_5$ perovskite (see Fig. 8a) nanocrystal scintillator has been successfully synthesized in solution by a method at low-temperature, based on which a novel optical fiber panel has been manufactured for high-quality X-ray CT imaging.[77] This Pb-free perovskite nano-scintillator has an adequate PLQY (59%) and extraordinary material stability in the ambient atmosphere for over three months. It also possesses a high scintillation LY, four times higher than the $CsPbBr_3$ nanocrystal counterpart at 80 kV, 70 μA (Fig. 8b). To test its potential application in practical clinic imaging, a $Cs_3Cu_2I_5$ nano-scintillator based X-ray detecting system has been constructed (Fig. 8c–e). A high-resolution projection image of the interior structure for a chip (Fig. 8f) and a three-dimensional CT image of a snail subject (Fig. 8g–j) can be obtained from this $Cs_3Cu_2I_5$ scintillator-based X-ray detector, exhibiting its promising application prospect for commercial X-ray scintillation

imaging. The $Cs_3Cu_2I_5$ scintillator has a quite fast response, and a short decay time of 38.94 ns has been achieved (Fig. 8k), making it capable for clinic radiography including CT.

It has been also reported that the scintillation performance of low-dimensional Pb-free perovskite nanocrystal can be improved a lot by doping methods. In a recent report, Tl$^+$ has been successfully doped into the host lattice of 0D perovskite $Cs_3Cu_2I_5$ for the growth of crystal ingot (Fig. 9a), based on which a scintillator-based detecting platform are expected to be established for X-ray/γ-ray detection.[112] Under X-ray radiation, the $Cs_3Cu_2I_5$:Tl$^+$ scintillator has an enhanced PLQY of 79.2% (Fig. 9b), and its RL includes a self-trapped exciton (STE) emission peaked at 440 nm (Fig. 9c) as well as a Tl$^+$-centre emission peaked at 510 nm (Fig. 9d). With Tl$^+$ doped, a steady-state scintillation LY of 150 000 photons per MeV can be obtained, approximately five times more than that of the undoped counterpart.[116] An outstanding energy resolution of 3.4 ± 0.2% at 662 keV (Fig. 9e) and a high LY of 87 000 photons per MeV (Fig. 9f) have been also achieved. When the signal-to-noise ratio (SNR) is set to be two, the X-ray detection limit can be reduced from 103.6 nGy$_{air}$ S^{-1} (undoped) to 66.3 nGy$_{air}$ S^{-1} (Tl$^+$ doped) (Fig. 9g), much lower than the requirement of 5.5 μGy$_{air}$ S^{-1} in clinic diagnosis by X-ray imaging.[108] However, as indicated in Fig. 9h, the afterglow emission (0.17% at 10 ms) of Tl$^+$-doped $Cs_3Cu_2I_5$ single crystal is not preferable for high-speed CT scanning imaging.
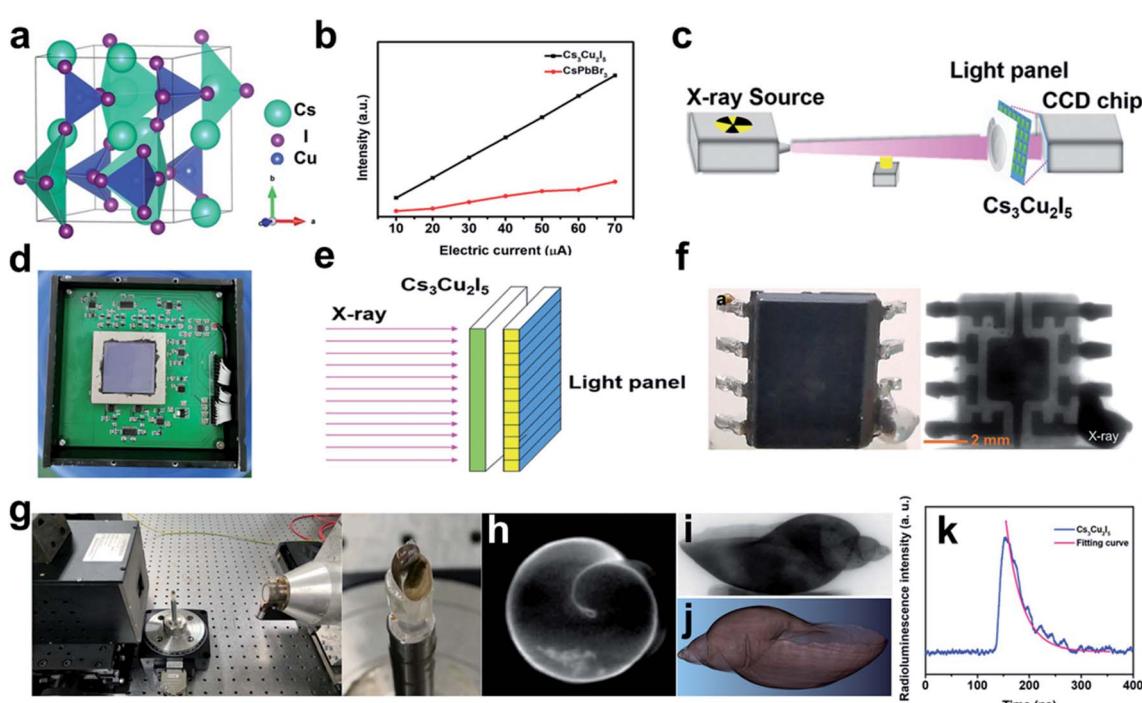
Fig. 8 (a) Crystal structure of the novel Pb-free perovskite $Cs_3Cu_2I_5$. (b) The comparison in LY of $CsPbBr_3$ quantum dots and $Cs_3Cu_2I_5$ nanocrystal under X-ray radiation. (c) Schematic description of the $Cs_3Cu_2I_5$-based equipment for X-ray scintillation imaging. (d) The photograph of Charge Coupled Device (CCD) chip. (e) Schematic depiction of the $Cs_3Cu_2I_5$-based X-ray scintillation imaging. (f) The image of chip obtained through the proposed device. (g) The proposed apparatus and the subject snail. The CT imaging apparatus includes an X-ray radiation source and the $Cs_3Cu_2I_5$ scintillator-based detector. (h) The projection image of the subject snail. (i) The reconstructed slice image of the subject snail. (j) The volume rendering of the subject snail. (k) The RL decay curve of $Cs_3Cu_2I_5$ nanocrystal. Reproduced with permission.[77] Copyright 2021 Wiley-VCH.
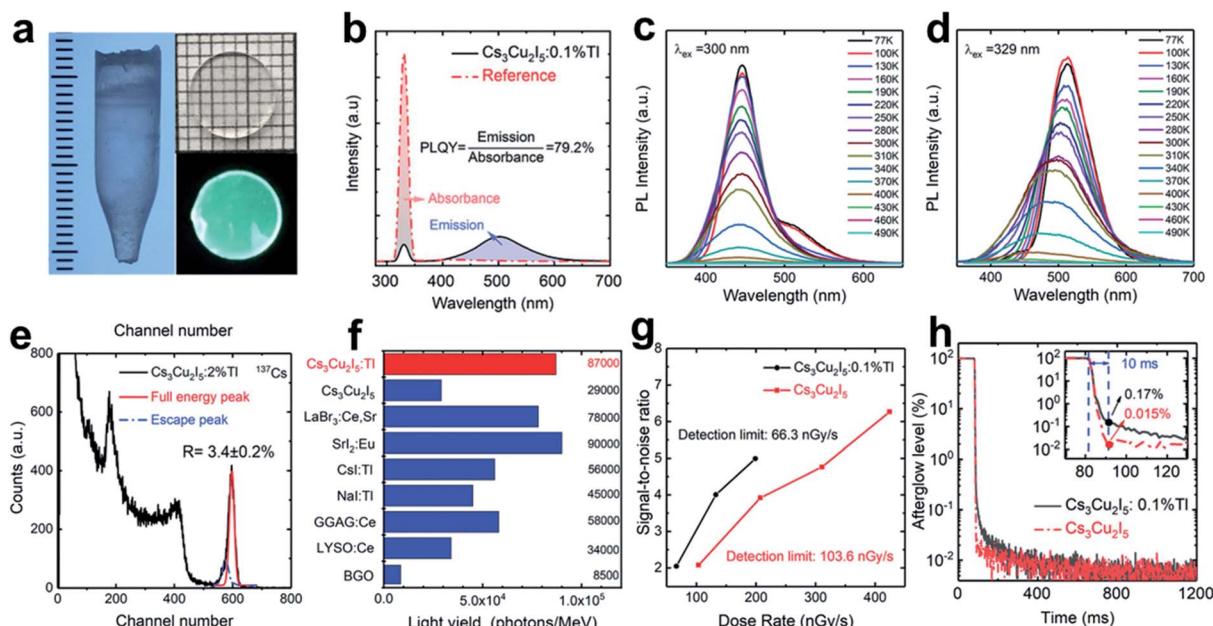
Fig. 9 (a) A $Cs_3Cu_2I_5$:Tl^+ crystal ingot grown in 7 mm diameter as well as a 1 mm thick panel under natural (up) and UV light (down). (b) PLQY profile of the 0.1%Tl^+ doped-$Cs_3Cu_2I_5$ single crystal. (c and d) Temperature dependent photoluminescence spectra for 0.1%Tl^+ doped-$Cs_3Cu_2I_5$ (77–490 K): (c) STE and (d) Tl^+-centre emission respectively. (e) Pulse height profile of 2% Tl^+-doped $Cs_3Cu_2I_5$ obtained from ^{137}Cs radiation source. (f) Comparisons in absolute LY between Tl^+-doped and pure $Cs_3Cu_2I_5$, and other typical scintillation materials. (g) Comparison in SNR as a function of X-ray dose rate for 0.1%Tl^+-doped and pure $Cs_3Cu_2I_5$. (h) Afterglow curves for 0.1% Tl^+-doped and pure $Cs_3Cu_2I_5$.[112] Copyright 2021 Wiley-VCH.

5. Challenges and outlook

In this work, we have comprehensively summarized the recent research achievements in all-inorganic perovskite nanocrystal for X-ray scintillation imaging. The significant advances cover the traditional heavy-metal based compounds (NaI:Tl^+/CsI:Tl^+, CWO, BGO, LSO, and LYSO), the latest perovskite scintillators $CsPbX_3$ (X= Cl, Br, I, or mixed-halides) as well as the Pb-free perovskite scintillators, which especially emphasizes the clinical applications. In terms of material morphology, nanoscale perovskites exhibit superior scintillation performance at room temperature when compared with bulk single crystals. The rapid development of nanotechnology further boosts the modification in X-ray scintillation behaviour for perovskite nano-scintillators, and then realizes satisfactory energy accumulation under low-dose exposure. The scintillation properties of perovskite nano-scintillators can be tuned by doping, bandgap engineering, or other material modification techniques to satisfy various application scenarios, but challenges still remain especially in the aspect of the stability in air and the toxicity of Pb^{2+}.

Encapsulation operations are essential to consider for maintaining the long-term stability of halide-perovskite nanomaterials in ambient air. To address the pollution problems caused by poisonous Pb^{2+}, a series of Pb-free halide perovskites like $A_3Bi_2X_9$ (A = Cs^+ or Rb^+), Rb_2CuBr_3, Cs_2-$AgBiBr_6$, and $Cs_2NaTbCl_6$ have been successfully synthesized to serve as potential substitutes for X-ray scintillation. But unfortunately, the scintillation performances of these Pb-free

perovskites are still not competitive to that of Pb-halide perovskites. Consequently, persistent attempts are made to promote their scintillation performance, including trials on new crystal-growth techniques and developments on novel perovskite nanocrystal with new substitutes for Pb^{2+}. At present, the halide-perovskite nanocrystal-based scintillation devices are still staying in laboratory-scale manufacturing. With a refractive index of approaching 1.0 for the general lens, X-rays are very difficult to be focused. Thus, manufacturing a large-area scintillation wafer/thin-film layer comparable to the size of the imaged subject is essential.[117] In addition, the material reproducibility and toxicity removal technology of halide-perovskite scintillators also become recent research hotspots that ultimately orientate to realize commercialized production.

In typical X-ray detectors, the scintillation layer is required to be thick enough for sufficient absorption on incident radiations. As for X-ray imaging on nonplanar surfaces, the flexibility under a certain thickness is another key criterion for building the scintillation layer of detection devices. The fabrication of a large-sized scintillation layer with good flexibility can be solved by the successful preparation of perovskite films, whereas, maintaining stable material quality under adequate thickness is still a tough technical problem. For instance, for adequate X-ray absorption (22 keV) by $(NH_4)_3Bi_2I_9$ layer, a thickness of at least 2 mm is required, but current film-deposition technology cannot satisfy this material requirement.[118] Thus, maintaining material thickness and flexibility in the large-area

film is a breakthrough point for the further advancement of perovskite scintillators.

Due to the high penetrating power of NIR light in animal organs/tissues, shifting the emitting light of contrast medium to the higher biological window has been a research hotspot for high-penetration bio-imaging and photodynamic therapy (PDT).[37] Down-converting incident X-ray to NIR emission will also be a promising research area to be explored in practical scintillation applications especially in high-radiation fields. The Cherenkov light appearing in UV/visible region will become a severe noise signal if the X-ray scintillating emission locates in the same spectral range, and what's worse, the original colour of optical fibres will gradually be changed due to the long-term absorption of UV/visible light.[119] Thus, finding ways to develop novel NIR emission scintillators to avoid radiation damage and reduce the noise signal is of great significance for commercialized applications. Besides co-doping methods, the native point defects tuned NIR emission is also very promising for scintillation wavelength control if the electron-transition energy gaps in the NIR range between defect states can be precisely predicted by computational simulation on electronic properties.[37]

The self-absorption effect is another adverse factor that causes severe reduction of light output. An enlarged Stokes shift will lead to a better separation between the absorption and emission spectrum, offering us an effective method to restrain the self-absorption. For instance, the $CsPbBr_3$ nanocrystal can serve as a sensitizer for organic dyes with large Stokes shift to realize a scintillation performance that almost eliminates the self-absorption effect, but unfortunately suffers a low light output of 9000 photons per MeV.[120] Thus, finding ways to improve the light output of the perovskite nanocrystal sensitized organic dyes will be another research hotpot. Doping technology has been widely applied for the modulation of perovskite scintillators, by which the Stokes shift can also be enlarged.[121] Relying on the ET process, the energy states of transition-metal/RE doping ions can act as the recombination center to produce scintillation emission with the wavelength corresponding to the transition gap.[37] Addition to these doping levels, the native defect states within the bandgap also exhibit the potential to control the scintillation performance.[37,64,122] The electronic properties of these intrinsic defects calculated through density functional theory can serve as a reliable theoretical instruction for future studies on defect-tuned scintillators.

Conflicts of interest

There are no conflicts to declare.

Acknowledgements

Notes and references

1 F. Cao, D. Yu, W. Ma, X. Xu, B. Cai, Y. M. Yang, S. Liu, L. He, Y. Ke, S. Lan, K.-L. Choy and H. Zeng, Shining Emitter in a Stable Host: Design of Halide Perovskite Scintillators for X-ray Imaging from Commercial Concept, *ACS Nano*, 2020, **14**(5), 5183–5193.

2 M. Nikl, Scintillation detectors for X-rays, *Meas. Sci. Technol.*, 2006, **17**(4), R37–R54.

3 L. Lu, M. Sun, Q. Lu, T. Wu and B. Huang, High energy X-ray radiation sensitive scintillating materials for medical imaging, cancer diagnosis and therapy, *Nano Energy*, 2021, **79**, 105437.

4 Y. Zhou, J. Chen, O. M. Bakr and O. F. Mohammed, Metal Halide Perovskites for X-ray Imaging Scintillators and Detectors, *ACS Energy Lett.*, 2021, **6**(2), 739–768.

5 J. Cao, Z. Guo, S. Zhu, Y. Fu, H. Zhang, Q. Wang and Z. Gu, Preparation of Lead-free Two-Dimensional-Layered $(C_8H_{17}NH_3)_2SnBr_4$ Perovskite Scintillators and Their Application in X-ray Imaging, *ACS Appl. Mater. Interfaces*, 2020, **12**(17), 19797–19804.

6 M. Overdick, C. Baumer, K. J. Engel, J. Fink, C. Herrmann, H. Kruger, M. Simon, R. Steadman and G. Zeitler, Status of Direct Conversion Detectors for Medical Imaging With X-Rays, *IEEE Trans. Nucl. Sci.*, 2009, **56**(4), 1800–1809.

7 S. O. Kasap and J. A. Rowlands, Direct-conversion flat-panel X-ray image sensors for digital radiography, *Proc. IEEE*, 2002, **90**(4), 591–604.

8 H. Wei, D. DeSantis, W. Wei, Y. Deng, D. Guo, T. J. Savenije, L. Cao and J. Huang, Dopant compensation in alloyed $CH_3NH_3PbBr_{3-x}Cl_x$ perovskite single crystals for gamma-ray spectroscopy, *Nat. Mater.*, 2017, **16**(8), 826–833.

9 W. Wolszczak, K. W. Krämer and P. Dorenbos, Engineering near-infrared emitting scintillators with efficient $Eu^{2+} \rightarrow Sm^{2+}$ energy transfer, *J. Lumin.*, 2020, **222**, 117101.

10 H. Wei and J. Huang, Halide lead perovskites for ionizing radiation detection, *Nat. Commun.*, 2019, **10**(1), 1066.

11 M. Lowdon, P. G. Martin, M. W. J. Hubbard, M. P. Taggart, D. T. Connor, Y. Verbelen, P. J. Sellin and T. B. Scott, Evaluation of Scintillator Detection Materials for Application within Airborne Environmental Radiation Monitoring, *Sensors*, 2019, **19**(18), 3828.

12 G. F. Knoll, *Radiation Detection and Measurement*, Wiley, New York 2000.

13 P. Lecoq, Development of new scintillators for medical applications, *Nucl. Instrum. Methods Phys. Res., Sect. A*, 2016, **809**, 130–139.

14 C. W. E. v. Eijk, Inorganic scintillators in medical imaging, *Phys. Med. Biol.*, 2002, **47**(8), R85–R106.

15 Q. Chen, J. Wu, X. Ou, B. Huang, J. Almutlaq, A. A. Zhumekenov, X. Guan, S. Han, L. Liang, Z. Yi, J. Li, X. Xie, Y. Wang, Y. Li, D. Fan, D. B. L. Teh, A. H. All, O. F. Mohammed, O. M. Bakr, T. Wu, M. Bettinelli, H. Yang, W. Huang and X. Liu, All-inorganic perovskite nanocrystal scintillators, *Nature*, 2018, **561**(7721), 88–93.

16 M. Nikl and A. Yoshikawa, Recent R&D Trends in Inorganic Single-Crystal Scintillator Materials for Radiation Detection, *Adv. Opt. Mater.*, 2015, **3**(4), 463–481.

17 F. Maddalena, L. Tjahjana, A. Xie, Arramel, S. Zeng, H. Wang, P. Coquet, W. Drozdowski, C. Dujardin, C. Dang and M. Birowosuto, Inorganic, Organic, and Perovskite Halides with Nanotechnology for High-Light Yield X- and γ-ray Scintillators, *Crystals*, 2019, **9**(2), 88.

18 M. Spahn, X-ray detectors in medical imaging, *Nucl. Instrum. Methods Phys. Res., Sect. A*, 2013, **731**, 57–63.

19 J. A. Rowlands, Material change for X-ray detectors, *Nature*, 2017, **550**(7674), 47–48.

20 M. D. Birowosuto, D. Cortecchia, W. Drozdowski, K. Brylew, W. Lachmanski, A. Bruno and C. Soci, X-ray Scintillation in Lead Halide Perovskite Crystals, *Sci. Rep.*, 2016, **6**(1), 37254.

21 D. Shi, V. Adinolfi, R. Comin, M. Yuan, E. Alarousu, A. Buin, Y. Chen, S. Hoogland, A. Rothenberger, K. Katsiev, Y. Losovyj, X. Zhang, P. A. Dowben, O. F. Mohammed, E. H. Sargent and O. M. Bakr, Low trap-state density and long carrier diffusion in organolead trihalide perovskite single crystals, *Science*, 2015, **347**(6221), 519.

22 B. Murali, E. Yengel, C. Yang, W. Peng, E. Alarousu, O. M. Bakr and O. F. Mohammed, The Surface of Hybrid Perovskite Crystals: A Boon or Bane, *ACS Energy Lett.*, 2017, **2**(4), 846–856.

23 S. D. Stranks, G. E. Eperon, G. Grancini, C. Menelaou, M. J. P. Alcocer, T. Leijtens, L. M. Herz, A. Petrozza and H. J. Snaith, Electron-Hole Diffusion Lengths Exceeding 1 Micrometer in an Organometal Trihalide Perovskite Absorber, *Science*, 2013, **342**(6156), 341.

24 N. Pradhan, Tips and Twists in Making High Photoluminescence Quantum Yield Perovskite Nanocrystals, *ACS Energy Lett.*, 2019, **4**(7), 1634–1638.

25 Z.-J. Yong, S.-Q. Guo, J.-P. Ma, J.-Y. Zhang, Z.-Y. Li, Y.-M. Chen, B.-B. Zhang, Y. Zhou, J. Shu, J.-L. Gu, L.-R. Zheng, O. M. Bakr and H.-T. Sun, Doping-Enhanced Short-Range Order of Perovskite Nanocrystals for Near-Unity Violet Luminescence Quantum Yield, *J. Am. Chem. Soc.*, 2018, **140**(31), 9942–9951.

26 A. N. Belsky, P. Chevallier, P. Dhez, P. Martin, C. Pédrini and A. N. Vasil'ev, X-ray excitation of luminescence of scintillator materials in the 7–22 keV region, *Nucl. Instrum. Methods Phys. Res., Sect. A*, 1995, **361**(1), 384–387.

27 W. Zhu, W. Ma, Y. Su, Z. Chen, X. Chen, Y. Ma, L. Bai, W. Xiao, T. Liu, H. Zhu, X. Liu, H. Liu, X. Liu and Y. Yang, Low-dose real-time X-ray imaging with nontoxic double perovskite scintillators, *Light: Sci. Appl.*, 2020, **9**(1), 112.

28 L. Chu, W. Ahmad, W. Liu, J. Yang, R. Zhang, Y. Sun, J. Yang and X. a. Li, Lead-Free Halide Double Perovskite Materials: A New Superstar Toward Green and Stable Optoelectronic Applications, *Nano-Micro Lett.*, 2019, **11**(1), 16.

29 J. Luo, X. Wang, S. Li, J. Liu, Y. Guo, G. Niu, L. Yao, Y. Fu, L. Gao, Q. Dong, C. Zhao, M. Leng, F. Ma, W. Liang, L. Wang, S. Jin, J. Han, L. Zhang, J. Etheridge, J. Wang, Y. Yan, E. H. Sargent and J. Tang, Efficient and stable emission of warm-white light from lead-free halide double perovskites, *Nature*, 2018, **563**(7732), 541–545.

30 B. Yang, L. Yin, G. Niu, J. H. Yuan, K. H. Xue, Z. Tan, X. S. Miao, M. Niu, X. Du, H. Song, E. Lifshitz and J. Tang, Lead-Free Halide Rb_2CuBr_3 as Sensitive X-Ray Scintillator, *Adv. Mater.*, 2019, **31**(44), e1904711.

31 T. Jun, K. Sim, S. Iimura, M. Sasase, H. Kamioka, J. Kim and H. Hosono, Lead-Free Highly Efficient Blue-Emitting $Cs_3Cu_2I_5$ with 0D Electronic Structure, *Adv. Mater.*, 2018, **30**(43), 1804547.

32 J.-L. Xie, Z.-Q. Huang, B. Wang, W.-J. Chen, W.-X. Lu, X. Liu and J.-L. Song, New lead-free perovskite $Rb_7Bi_3Cl_{16}$ nanocrystals with blue luminescence and excellent moisture-stability, *Nanoscale*, 2019, **11**(14), 6719–6726.

33 Q. Hu, Z. Deng, M. Hu, A. Zhao, Y. Zhang, Z. Tan, G. Niu, H. Wu and J. Tang, X-ray scintillation in lead-free double perovskite crystals, *Sci. China: Chem.*, 2018, **61**(12), 1581–1586.

34 E. Shefer, A. Altman, R. Behling, R. Goshen, L. Gregorian, Y. Roterman, I. Uman, N. Wainer, Y. Yagil and O. Zarchin, State of the Art of CT Detectors and Sources: A Literature Review, *Curr. Radiol. Rep.*, 2013, **1**(1), 76–91.

35 S. Liu, X. Feng, M. Nikl, L. Wu, Z. Zhou, J. Li, H. Kou, Y. Zeng, Y. Shi and Y. Pan, Fabrication and Scintillation Performance of Nonstoichiometric LuAG:Ce Ceramics, *J. Am. Ceram. Soc.*, 2015, **98**(2), 510–514.

36 P. Lecoq, A. Gektin and M. Korzhik, *Scintillation Mechanisms in Inorganic Scintillators*, Springer International Publishing, 2017, pp. 125–174.

37 L. Lu, M. Sun, T. Wu, Q. Lu and B. Huang, Native point defect modulated Cr^{3+}-LaAlO$_3$ as an *in vitro* excited contrast medium for *in vivo* near-infrared persistent deep-tissue bio-imaging, *Chem. Commun.*, 2021, **57**(74), 9366–9369.

38 M. Sun, Q. He, X. Kuang, Q. Zhang, S. Ye and B. Huang, Probing oxide-ion conduction in low-temperature SOFCs, *Nano Energy*, 2018, **50**, 88–96.

39 M. Sun and B. Huang, "Energy Selection Channels" for High-Performance Electrolyte: Anion-Frenkel Defect Pair as Dominant Source for O Ion Conductions in Pyrochlore-type Lanthanide Hafnium Oxides SOFC, *Inorg. Chem.*, 2017, **56**(14), 7975–7984.

40 J. Wang, S. Bai, H. Zhang and C. Zhang, The structure, thermal expansion coefficient and sintering behavior of Nd^{3+}-doped $La_2Zr_2O_7$ for thermal barrier coatings, *J. Alloys Compd.*, 2009, **476**(1), 89–91.

41 B. Huang, R. Gillen and J. Robertson, Study of CeO_2 and Its Native Defects by Density Functional Theory with Repulsive Potential, *J. Phys. Chem. C*, 2014, **118**(42), 24248–24256.

42 J. Barranco, A. Méndez-Blas and M. E. Calixto, Structural, morphology and optical properties of $NaYF_4$ thin films doped with trivalent lanthanide ions, *J. Mater. Sci.: Mater. Electron.*, 2019, **30**(5), 4855–4866.

43 D. P. Karim and A. T. Aldred, Localized level hopping transport in $La(Sr)CrO_3$, *Phys. Rev. B: Condens. Matter Mater. Phys.*, 1979, **20**(6), 2255–2263.

44 A. S. John, M. G. Sol, W. T. Mark and T. Melvin, Study of afterglow in X-ray phosphors for use on fast-framing charge-coupled device detectors, *Opt. Eng.*, 1997, **36**(11), 3212–3222.

45 C. R. Stanek, K. J. McClellan, M. R. Levy and R. W. Grimes, Defect behavior in rare earth $REAlO_3$ scintillators, *J. Appl. Phys.*, 2006, **99**(11), 113518.

46 C. R. Stanek, M. R. Levy, K. J. McClellan, B. P. Uberuaga and R. W. Grimes, Defect identification and compensation in rare earth oxide scintillators, *Nucl. Instrum. Methods Phys. Res., Sect. B*, 2008, **266**(12), 2657–2664.

47 M. Fasoli, A. Vedda, M. Nikl, C. Jiang, B. P. Uberuaga, D. A. Andersson, K. J. McClellan and C. R. Stanek, Band-gap engineering for removing shallow traps in rare-earth $Lu_3Al_5O_{12}$ garnet scintillators using Ga^{3+} doping, *Phys. Rev. B: Condens. Matter Mater. Phys.*, 2011, **84**(8), 081102.

48 B. C. Grabmaier, Luminescent materials for medical application, *J. Lumin.*, 1994, **60–61**, 967–970.

49 S. Blahuta, B. Viana, A. Bessière, E. Mattmann and B. LaCourse, Luminescence quenching processes in Gd_2O_2S:Pr^{3+},Ce^{3+} scintillating ceramics, *Opt. Mater.*, 2011, **33**(10), 1514–1518.

50 M. Sun, H. Dong, A. W. Dougherty, Q. Lu, D. Peng, W.-T. Wong, B. Huang, L.-D. Sun and C.-H. Yan, Nanophotonic energy storage in upconversion nanoparticles, *Nano Energy*, 2019, **56**, 473–481.

51 H. Yamada, A. Suzuki, Y. Uchida, M. Yoshida, H. Yamamoto and Y. Tsukuda, A Scintillator Gd2O2S:Pr,Ce,F for X-Ray Computed Tomography, *J. Electrochem. Soc.*, 1989, **136**(9), 2713–2716.

52 T. Yanagida, Study of rare-earth-doped scintillators, *Opt. Mater.*, 2013, **35**(11), 1987–1992.

53 Y. Zhang, W. Jie, P. Chen, W. Liu and J. Hao, Ferroelectric and Piezoelectric Effects on the Optical Process in Advanced Materials and Devices, *Adv. Mater.*, 2018, **30**(34), 1707007.

54 J. Shamsi, A. S. Urban, M. Imran, L. De Trizio and L. Manna, Metal Halide Perovskite Nanocrystals: Synthesis, Post-Synthesis Modifications, and Their Optical Properties, *Chem. Rev.*, 2019, **119**(5), 3296–3348.

55 P. Schuster and E. Brubaker, Investigating the Anisotropic Scintillation Response in Anthracene through Neutron, Gamma-Ray, and Muon Measurements, *IEEE Trans. Nucl. Sci.*, 2016, **63**(3), 1942–1954.

56 Y. Wei, Z. Cheng and J. Lin, An overview on enhancing the stability of lead halide perovskite quantum dots and their applications in phosphor-converted LEDs, *Chem. Soc. Rev.*, 2019, **48**(1), 310–350.

57 H. Zhu, P. Zhang and S. Dai, Recent Advances of Lanthanum-Based Perovskite Oxides for Catalysis, *ACS Catal.*, 2015, **5**(11), 6370–6385.

58 F. Zhou, Z. Li, W. Lan, Q. Wang, L. Ding and Z. Jin, Halide Perovskite, a Potential Scintillator for X-Ray Detection, *Small Methods*, 2020, **4**(10), 2000506.

59 S. E. Derenzo, M. J. Weber, E. Bourret-Courchesne and M. K. Klintenberg, The quest for the ideal inorganic scintillator, *Nucl. Instrum. Methods Phys. Res., Sect. A*, 2003, **505**(1), 111–117.

60 W. Huda and R. B. Abrahams, X-Ray-Based Medical Imaging and Resolution, *Am. J. Roentgenol.*, 2015, **204**(4), W393–W397.

61 S. J. Duclos, C. D. Greskovich, R. J. Lyons, J. S. Vartuli, D. M. Hoffman, R. J. Riedner and M. J. Lynch, Development of the HiLightTM scintillator for computed tomography medical imaging, *Nucl. Instrum. Methods Phys. Res., Sect. A*, 2003, **505**(1), 68–71.

62 H. Chen, M. M. Rogalski and J. N. Anker, Advances in functional X-ray imaging techniques and contrast agents, *Phys. Chem. Chem. Phys.*, 2012, **14**(39), 13469–13486.

63 C. Ronda, H. Wieczorek, V. Khanin and P. Rodnyi, Review-Scintillators for Medical Imaging: A Tutorial Overview, *ECS J. Solid State Sci. Technol.*, 2016, **5**(1), R3121–R3125.

64 X. Ou, X. Qin, B. Huang, J. Zan, Q. Wu, Z. Hong, L. Xie, H. Bian, Z. Yi, X. Chen, Y. Wu, X. Song, J. Li, Q. Chen, H. Yang and X. Liu, High-resolution X-ray luminescence extension imaging, *Nature*, 2021, **590**(7846), 410–415.

65 M. S. Alekhin, J. T. M. d. Haas, K. W. Krämer, I. V. Khodyuk, L. d. Vries and P. Dorenbos, Scintillation properties and self absorption in SrI_2:Eu^{2+}, in *IEEE Nuclear Science Symposium & Medical Imaging Conference*, 30 Oct.-6 Nov. 2010, 2010, pp. 1589–1599.

66 M. S. Alekhin, D. A. Biner, K. W. Krämer and P. Dorenbos, Optical and scintillation properties of $CsBa_2I_5$:Eu^{2+}, *J. Lumin.*, 2014, **145**, 723–728.

67 C. Dujardin, E. Auffray, E. Bourret-Courchesne, P. Dorenbos, P. Lecoq, M. Nikl, A. N. Vasil'ev, A. Yoshikawa and R. Zhu, Needs, Trends, and Advances in Inorganic Scintillators, *IEEE Trans. Nucl. Sci.*, 2018, **65**(8), 1977–1997.

68 R. H. P. Awater, M. S. Alekhin, D. A. Biner, K. W. Krämer and P. Dorenbos, Converting SrI_2:Eu^{2+} into a near infrared scintillator by Sm^{2+} co-doping, *J. Lumin.*, 2019, **212**, 1–4.

69 W. Wolszczak, K. W. Krämer and P. Dorenbos, $CsBa_2I_5$:Eu^{2+},Sm^{2+}-The First High-Energy Resolution Black Scintillator for γ-Ray Spectroscopy, *Phys. Status Solidi RRL*, 2019, **13**(9), 1900158.

70 K. Lin, J. Xing, L. N. Quan, F. P. G. de Arquer, X. Gong, J. Lu, L. Xie, W. Zhao, D. Zhang, C. Yan, W. Li, X. Liu, Y. Lu, J. Kirman, E. H. Sargent, Q. Xiong and Z. Wei, Perovskite light-emitting diodes with external quantum efficiency exceeding 20 per cent, *Nature*, 2018, **562**(7726), 245–248.

71 Q. A. Akkerman and L. Manna, What Defines a Halide Perovskite?, *ACS Energy Lett.*, 2020, **5**(2), 604–610.

72 S. D. Stranks and H. J. Snaith, Metal-halide perovskites for photovoltaic and light-emitting devices, *Nat. Nanotechnol.*, 2015, **10**, 391.

73 Y. Zhang, R. Sun, X. Ou, K. Fu, Q. Chen, Y. Ding, L.-J. Xu, L. Liu, Y. Han, A. V. Malko, X. Liu, H. Yang, O. M. Bakr, H. Liu and O. F. Mohammed, Metal Halide Perovskite Nanosheet for X-ray High-Resolution Scintillation Imaging Screens, *ACS Nano*, 2019, **13**(2), 2520–2525.

74 J.-P. Correa-Baena, M. Saliba, T. Buonassisi, M. Grätzel, A. Abate, W. Tress and A. Hagfeldt, Promises and

challenges of perovskite solar cells, *Science*, 2017, **358**(6364), 739–744.

75 C. W. E. van Eijk, Inorganic scintillators in medical imaging detectors, *Nucl. Instrum. Methods Phys. Res., Sect. A*, 2003, **509**(1), 17–25.

76 B. Yang, L. Yin, G. Niu, J.-H. Yuan, K.-H. Xue, Z. Tan, X.-S. Miao, M. Niu, X. Du, H. Song, E. Lifshitz and J. Tang, Lead-Free Halide Rb_2CuBr_3 as Sensitive X-Ray Scintillator, *Adv. Mater.*, 2019, **31**(44), 1904711.

77 J. Zhou, K. An, P. He, J. Yang, C. Zhou, Y. Luo, W. Kang, W. Hu, P. Feng, M. Zhou and X. Tang, Solution-Processed Lead-Free Perovskite Nanocrystal Scintillators for High-Resolution X-Ray CT Imaging, *Adv. Opt. Mater.*, 2021, **9**(11), 2002144.

78 A. H. Slavney, R. W. Smaha, I. C. Smith, A. Jaffe, D. Umeyama and H. I. Karunadasa, Chemical Approaches to Addressing the Instability and Toxicity of Lead-Halide Perovskite Absorbers, *Inorg. Chem.*, 2017, **56**(1), 46–55.

79 L. Song, P.-P. Li, W. Yang, X.-H. Lin, H. Liang, X.-F. Chen, G. Liu, J. Li and H.-H. Yang, Low-Dose X-ray Activation of W(VI)-Doped Persistent Luminescence Nanoparticles for Deep-Tissue Photodynamic Therapy, *Adv. Funct. Mater.*, 2018, **28**(18), 1707496.

80 L. Sudheendra, G. K. Das, C. Li, D. Stark, J. Cena, S. Cherry and I. M. Kennedy, $NaGdF_4:Eu^{3+}$ Nanoparticles for Enhanced X-ray Excited Optical Imaging, *Chem. Mater.*, 2014, **26**(5), 1881–1888.

81 Y. Li, M. Gecevicius and J. Qiu, Long persistent phosphors-from fundamentals to applications, *Chem. Soc. Rev.*, 2016, **45**(8), 2090–2136.

82 C.-C. Hsu, S.-L. Lin and C. A. Chang, Lanthanide-Doped Core–Shell–Shell Nanocomposite for Dual Photodynamic Therapy and Luminescence Imaging by a Single X-ray Excitation Source, *ACS Appl. Mater. Interfaces*, 2018, **10**(9), 7859–7870.

83 C. B. Lushchik, CHAPTER 8 – Creation of Frenkel Defect Pairs by Excitons in Alkali Halides, in *Modern Problems in Condensed Matter Sciences*, ed. R. A. Johnson and A. N. Orlov, Elsevier, 1986, vol. 13, pp. 473–525.

84 C. Dong, X. Han, W. Li, Q. Qiu and J. Wang, Anti-solvent assisted multi-step deposition for efficient and stable carbon-based $CsPbI_2Br$ all-inorganic perovskite solar cell, *Nano Energy*, 2019, **59**, 553–559.

85 L. Wang, H. Zhou, J. Hu, B. Huang, M. Sun, B. Dong, G. Zheng, Y. Huang, Y. Chen, L. Li, Z. Xu, N. Li, Z. Liu, Q. Chen, L.-D. Sun and C.-H. Yan, A Eu^{3+}–Eu^{2+} ion redox shuttle imparts operational durability to Pb–I perovskite solar cells, *Science*, 2019, **363**(6424), 265–270.

86 L. Li, S. Ye, J. Qu, F. Zhou, J. Song and G. Shen, Recent Advances in Perovskite Photodetectors for Image Sensing, *Small*, 2021, **17**(18), 2005606.

87 H. Wu, Y. Ge, G. Niu and J. Tang, Metal Halide Perovskites for X-Ray Detection and Imaging, *Matter*, 2021, **4**(1), 144–163.

88 Z. Li, F. Zhou, H. Yao, Z. Ci, Z. Yang and Z. Jin, Halide perovskites for high-performance X-ray detector, *Mater. Today*, 2021, **48**, 155–175.

89 J. Liu, B. Shabbir, C. Wang, T. Wan, Q. Ou, P. Yu, A. Tadich, X. Jiao, D. Chu, D. Qi, D. Li, R. Kan, Y. Huang, Y. Dong, J. Jasieniak, Y. Zhang and Q. Bao, Flexible, Printable Soft-X-Ray Detectors Based on All-Inorganic Perovskite Quantum Dots, *Adv. Mater.*, 2019, **31**(30), 1901644.

90 L. Clinckemalie, D. Valli, M. B. J. Roeffaers, J. Hofkens, B. Pradhan and E. Debroye, Challenges and Opportunities for $CsPbBr_3$ Perovskites in Low- and High-Energy Radiation Detection, *ACS Energy Lett.*, 2021, **6**(4), 1290–1314.

91 E. H. Jung, N. J. Jeon, E. Y. Park, C. S. Moon, T. J. Shin, T.-Y. Yang, J. H. Noh and J. Seo, Efficient, stable and scalable perovskite solar cells using poly(3-hexylthiophene), *Nature*, 2019, **567**(7749), 511–515.

92 Q. Jiang, Y. Zhao, X. Zhang, X. Yang, Y. Chen, Z. Chu, Q. Ye, X. Li, Z. Yin and J. You, Surface passivation of perovskite film for efficient solar cells, *Nat. Photonics*, 2019, **13**(7), 460–466.

93 G. M. Kim, A. Ishii, S. Öz and T. Miyasaka, MACl-Assisted Ge Doping of Pb-Hybrid Perovskite: A Universal Route to Stabilize High Performance Perovskite Solar Cells, *Adv. Energy Mater.*, 2020, **10**(7), 1903299.

94 C. Liu, W. Li, C. Zhang, Y. Ma, J. Fan and Y. Mai, All-Inorganic $CsPbI_2Br$ Perovskite Solar Cells with High Efficiency Exceeding 13%, *J. Am. Chem. Soc.*, 2018, **140**(11), 3825–3828.

95 W. Ahmad, J. Khan, G. Niu and J. Tang, Inorganic $CsPbI_3$ Perovskite-Based Solar Cells: A Choice for a Tandem Device, *Sol. RRL*, 2017, **1**(7), 1700048.

96 L. Gao and Q. Yan, Recent Advances in Lead Halide Perovskites for Radiation Detectors, *Sol. RRL*, 2020, **4**(2), 1900210.

97 M. Kobayashi, K. Omata, S. Sugimoto, Y. Tamagawa, T. Kuroiwa, H. Asada, H. Takeuchi and S. Kondo, Scintillation characteristics of $CsPbCl_3$ single crystals, *Nucl. Instrum. Methods Phys. Res., Sect. A*, 2008, **592**(3), 369–373.

98 V. B. Mykhaylyk, H. Kraus, V. Kapustianyk, H. J. Kim, P. Mercere, M. Rudko, P. Da Silva, O. Antonyak and M. Dendebera, Bright and fast scintillations of an inorganic halide perovskite $CsPbBr_3$ crystal at cryogenic temperatures, *Sci. Rep.*, 2020, **10**(1), 8601.

99 L. Protesescu, S. Yakunin, M. I. Bodnarchuk, F. Krieg, R. Caputo, C. H. Hendon, R. X. Yang, A. Walsh and M. V. Kovalenko, Nanocrystals of Cesium Lead Halide Perovskites ($CsPbX_3$, X = Cl, Br, and I): Novel Optoelectronic Materials Showing Bright Emission with Wide Color Gamut, *Nano Lett.*, 2015, **15**(6), 3692–3696.

100 M. D. Birowosuto, D. Cortecchia, W. Drozdowski, K. Brylew, W. Lachmanski, A. Bruno and C. Soci, X-ray Scintillation in Lead Halide Perovskite Crystals, *Sci. Rep.*, 2016, **6**, 37254.

101 M. J. Weber, Inorganic scintillators: today and tomorrow, *J. Lumin.*, 2002, **100**(1), 35–45.

102 S. Khalfin and Y. Bekenstein, Advances in lead-free double perovskite nanocrystals, engineering band-gaps and enhancing stability through composition tunability, *Nanoscale*, 2019, **11**(18), 8665–8679.

103 N. Phung and A. Abate, The Impact of Nano- and Microstructure on the Stability of Perovskite Solar Cells, *Small*, 2018, **14**(46), 1802573.

104 G. Pan, X. Bai, D. Yang, X. Chen, P. Jing, S. Qu, L. Zhang, D. Zhou, J. Zhu, W. Xu, B. Dong and H. Song, Doping Lanthanide into Perovskite Nanocrystals: Highly Improved and Expanded Optical Properties, *Nano Lett.*, 2017, **17**(12), 8005–8011.

105 C. Wang, H. Lin, Z. Zhang, Z. Qiu, H. Yang, Y. Cheng, J. Xu, X. Xiang, L. Zhang and Y. Wang, X-ray excited CsPb(Cl,Br)$_3$ perovskite quantum dots-glass composite with long-lifetime, *J. Eur. Ceram. Soc.*, 2020, **40**(5), 2234–2238.

106 Q. Xu, J. Wang, W. Shao, X. Ouyang, X. Wang, X. Zhang, Y. Guo and X. Ouyang, A solution-processed zero-dimensional all-inorganic perovskite scintillator for high resolution gamma-ray spectroscopy detection, *Nanoscale*, 2020, **12**(17), 9727–9732.

107 J. H. Heo, D. H. Shin, J. K. Park, D. H. Kim, S. J. Lee and S. H. Im, High-Performance Next-Generation Perovskite Nanocrystal Scintillator for Nondestructive X-Ray Imaging, *Adv. Mater.*, 2018, **30**(40), 1801743.

108 H. Wei, Y. Fang, P. Mulligan, W. Chuirazzi, H.-H. Fang, C. Wang, B. R. Ecker, Y. Gao, M. A. Loi, L. Cao and J. Huang, Sensitive X-ray detectors made of methylammonium lead tribromide perovskite single crystals, *Nat. Photonics*, 2016, **10**(5), 333–339.

109 R. Lin, Q. Guo, Q. Zhu, Y. Zhu, W. Zheng and F. Huang, All-Inorganic CsCu$_2$I$_3$ Single Crystal with High-PLQY ($\approx$15.7%) Intrinsic White-Light Emission *via* Strongly Localized 1D Excitonic Recombination, *Adv. Mater.*, 2019, **31**(46), 1905079.

110 L. Lian, M. Zheng, W. Zhang, L. Yin, X. Du, P. Zhang, X. Zhang, J. Gao, D. Zhang, L. Gao, G. Niu, H. Song, R. Chen, X. Lan, J. Tang and J. Zhang, Efficient and Reabsorption-Free Radioluminescence in Cs$_3$Cu$_2$I$_5$ Nanocrystals with Self-Trapped Excitons, *Adv. Sci.*, 2020, **7**(11), 2000195.

111 X. Zhao, T. Jin, W. Gao, G. Niu, J. Zhu, B. Song, J. Luo, W. Pan, H. Wu, M. Zhang, X. He, L. Fu, Z. Li, H. Zhao and J. Tang, Embedding Cs$_3$Cu$_2$I$_5$ Scintillators into Anodic Aluminum Oxide Matrix for High-Resolution X-Ray Imaging, *Adv. Opt. Mater.*, 2021, 2101194.

112 S. Cheng, M. Nikl, A. Beitlerova, R. Kucerkova, X. Du, G. Niu, Y. Jia, J. Tang, G. Ren and Y. Wu, Ultrabright and Highly Efficient All-Inorganic Zero-Dimensional Perovskite Scintillators, *Adv. Opt. Mater.*, 2021, **9**(13), 2100460.

113 K. M. McCall, C. C. Stoumpos, O. Y. Kontsevoi, G. C. B. Alexander, B. W. Wessels and M. G. Kanatzidis, From 0D Cs$_3$Bi$_2$I$_9$ to 2D Cs$_3$Bi$_2$I$_6$Cl$_3$: Dimensional Expansion Induces a Direct Band Gap but Enhances Electron-Phonon Coupling, *Chem. Mater.*, 2019, **31**(7), 2644–2650.

114 N. Ding, D. Zhou, G. Pan, W. Xu, X. Chen, D. Li, X. Zhang, J. Zhu, Y. Ji and H. Song, Europium-Doped Lead-Free Cs$_3$Bi$_2$Br$_9$ Perovskite Quantum Dots and Ultrasensitive Cu^{2+} Detection, *ACS Sustainable Chem. Eng.*, 2019, **7**(9), 8397–8404.

115 B. Yang, X. Mao, F. Hong, W. Meng, Y. Tang, X. Xia, S. Yang, W. Deng and K. Han, Lead-Free Direct Band Gap Double-Perovskite Nanocrystals with Bright Dual-Color Emission, *J. Am. Chem. Soc.*, 2018, **140**(49), 17001–17006.

116 S. Cheng, A. Beitlerova, R. Kucerkova, M. Nikl, G. Ren and Y. Wu, Zero-Dimensional Cs$_3$Cu$_2$I$_5$ Perovskite Single Crystal as Sensitive X-Ray and γ-Ray Scintillator, *Phys. Status Solidi RRL*, 2020, **14**(11), 2000374.

117 B. Yang, W. Pan, H. Wu, G. Niu, J.-H. Yuan, K.-H. Xue, L. Yin, X. Du, X.-S. Miao, X. Yang, Q. Xie and J. Tang, Heteroepitaxial passivation of Cs$_2$AgBiBr$_6$ wafers with suppressed ionic migration for X-ray imaging, *Nat. Commun.*, 2019, **10**(1), 1989.

118 R. Zhuang, X. Wang, W. Ma, Y. Wu, X. Chen, L. Tang, H. Zhu, J. Liu, L. Wu, W. Zhou, X. Liu and Y. Yang, Highly sensitive X-ray detector made of layered perovskite-like (NH$_4$)$_3$Bi$_2$I$_9$ single crystal with anisotropic response, *Nat. Photonics*, 2019, **13**(9), 602–608.

119 G. Okada, N. Kawaguchi and T. Yanagida, Development of near-infrared-emitting scintillators based on rare-earth-doped garnet crystals-Part 1, *Sens. Mater.*, 2017, **29**, 1407–1415.

120 M. Gandini, I. Villa, M. Beretta, C. Gotti, M. Imran, F. Carulli, E. Fantuzzi, M. Sassi, M. Zaffalon, C. Brofferio, L. Manna, L. Beverina, A. Vedda, M. Fasoli, L. Gironi and S. Brovelli, Efficient, fast and reabsorption-free perovskite nanocrystal-based sensitized plastic scintillators, *Nat. Nanotechnol.*, 2020, **15**(6), 462–468.

121 Y. Zhou, J. Chen, O. M. Bakr and H.-T. Sun, Metal-Doped Lead Halide Perovskites: Synthesis, Properties, and Optoelectronic Applications, *Chem. Mater.*, 2018, **30**(19), 6589–6613.

122 B. Huang, Native Point Defects in CaS: Focus on Intrinsic Defects and Rare Earth Ion Dopant Levels for Up-converted Persistent Luminescence, *Inorg. Chem.*, 2015, **54**(23), 11423–11440.